NASA Technical Memorandum 89421

Simulation of Transonic Viscous Wing and Wing-Fuselage Flows Using Zonal Methods

Jolen Flores

March 1987

National Aeronautics and
Space Administration

NASA Technical Memorandum 89421

Simulation of Transonic Viscous Wing and Wing-Fuselage Flows Using Zonal Methods

Jolen Flores, Ames Research Center, Moffett Field, California

March 1987

National Aeronautics and
Space Administration

Ames Research Center
Moffett Field, California 94035

SIMULATION OF TRANSONIC VISCOUS WING AND WING-FUSELAGE FLOWS USING ZONAL METHODS

JOLEN FLORES*

Abstract. The thin-layer Navier-Stokes equations are coupled with a zonal scheme (or domain-decomposition method) to develop the Transonic Navier-Stokes (TNS) wing-alone code. TNS has a total of 4 zones and is extended to a total of 16 zones for the wing-fuselage version of the code. Results are computed on the Cray X-MP-48 and compared with experimental data.

Key words. zonal methods, applied aerodynamics, computational fluid dynamics, transonic, viscous.

Running head: Zonal-Method Simulation of Transonic Flows

1. Introduction. With the improvement of numerical algorithms for the solution of the three-dimensional Euler/Navier-Stokes equations and the recent advancements in computer capabilities, previously unchallenged problems in computational fluid dynamics (CFD) are now being attempted. Some of the more recent transonic applications involving more sophistication in the geometries have appeared; they include Deiwert and Rothmund [9], Deiwert et al. [10], Fujii and Kutler [15], and Mansour [24]. However, even these solutions were conducted on coarse grids and required large amounts of cpu time, thereby precluding their use for more complicated geometries.

*Research Scientist, NASA Ames Research Center, Moffett Field, California 94035.

The next step in the advancement of CFD is in the simulation of transonic flow over complex geometries. However, generating a single grid in three dimensions for this simulation is one of the biggest pacing items in CFD. Currently, numerically generated grids in curvilinear coordinate systems are commonly used around arbitrary geometries. The implementation of the boundary conditions is easier on body-fitted systems. As the geometry becomes more complex, such as wing-body-strake or wing-canard combinations, the generation of a single grid becomes a very difficult task. Add to this the requirement of appropriate clustering of the grid points at all no-slip surfaces, and in regions of high gradient flow, and this task becomes nearly impossible.

To help alleviate this problem, zonal approaches have become increasingly popular. In the zonal approach, the flow field is partitioned into distinct "zones," each of which is solved independently. Using this approach, a coarse base grid can be generated about the geometry in question. Then the grid for any subdomain can be generated easily. Refined zones for regions of high gradients such as shear layers, shock waves, jets, wakes, and vortices can also be easily generated. As more components are added to the geometry, more zones can be added to capture the pertinent flow about them.

This zonal approach is not novel, having been used implicitly in the introduction of boundary-layer theory by Prandtl [25]. Here the flow field is divided into an inner viscous region where the boundary-layer equations are solved and matched with an outer inviscid solution. Thus, using this zonal approach, the boundary-layer equations could be solved via a marching technique while different relaxation methods are applied to the outer inviscid flow. Most noncomplex general viscous flows can be simulated without using the more consuming Navier-Stokes equations.

The zonal approach has a number of advantages: (i) the difficulties in generating three-dimensional grids for different types of complex configurations can be reduced with the use of zonal methods; (ii) different types of grid topologies can be implemented where appropriate in order for the grids to be mesh-efficient (that is, more points on the body surface where accuracy is desired, and fewer points in the flow field); (iii) different equations sets, with different algorithms, can be implemented in the various zones for computational efficiency; and (iv) information for only one zone need reside in the computer core at any given time, thereby relaxing memory limitations. Even in turbulence modeling, the zonal approach can be applied as described by Kline et al. [21]. In short, there is a wide variety of situations in which zonal methods can be applied with substantial gain.

Figure 1 illustrates the two major types of zonal interfaces, patched and overlapped. Earlier work in the development of a zonal-boundary scheme, for a system of hyperbolic equations includes that of Cambier et al. [6]. Further work on patched grids using the Euler equations was done by Rai [30], Hessenius and Pulliam [16], and Hessenius and Rai [17]. The patched grid concept was also used for the potential and full-potential equations by Lee et al. [22] and Yu [35]. The approach of overlapped grids was used with the Euler equations by Atta [1] and Atta and Vadyak [2]. Steger et al. [33] give results obtained on overlaid grids in conjunction with the stream-function approach. The current work uses the patched grid zoning method in a grid-refinement mode. Other work using this grid refinement mode has been done by Eriksson [11] and Baker et al. [3]. It is also possible with the zonal approach to solve different types of equation sets in the different zones [8].

This paper discusses the computational approach in which the fast-convergent, Pulliam-Chaussee [28] diagonal algorithm is coupled with a zonal

approach. The new approach permits relatively inexpensive fine-grid solutions to be made of the Euler/Navier-Stokes equations, which is especially important for flows with shock/boundary-layer interaction. Validation of the code by comparing numerical solutions with existing experimental data will also be presented.

2. Governing equations. The equations solved in this study are the Reynolds-averaged Navier-Stokes equations written in strong conservation-law form. These equations are simplified by using the standard thin-layer approximation for the viscous terms. The thin-layer Navier-Stokes equations written in generalized curvilinear coordinates are

$$\partial_\tau \hat{Q} + \partial_\xi \hat{E} + \partial_\eta \hat{F} + \partial_\zeta \hat{G} = Re^{-1} \partial_\zeta \hat{S} \,, \tag{1}$$

where

$$\hat{Q} = J^{-1} \begin{bmatrix} \rho \\ \rho u \\ \rho v \\ \rho w \\ e \end{bmatrix} \,, \quad \hat{E} = J^{-1} \begin{bmatrix} \rho U \\ \rho u U + \xi_x p \\ \rho v U + \xi_y p \\ \rho w U + \xi_z p \\ U(e + p) - \xi_t p \end{bmatrix}$$

$$\hat{F} = J^{-1} \begin{bmatrix} \rho V \\ \rho u V + \eta_x p \\ \rho v V + \eta_y p \\ \rho w V + \eta_z p \\ V(e + p) - \eta_t p \end{bmatrix} \,, \quad \hat{G} = J^{-1} \begin{bmatrix} \rho W \\ \rho u W + \zeta_x p \\ \rho v W + \zeta_y p \\ \rho w W + \zeta_z p \\ W(e + p) - \zeta_t p \end{bmatrix} \,,$$

with

$$U = \xi_t + \xi_x u + \xi_y v + \xi_z w$$

$$V = \eta_t + \eta_x u + \eta_y v + \eta_z w$$

$$W = \zeta_t + \zeta_x u + \zeta_y v + \zeta_z w$$

and

$$\hat{S} = J^{-1}\begin{bmatrix} 0 \\ \mu m_1 u_\zeta + (\mu/3) m_2 \zeta_x \\ \mu m_1 v_\zeta + (\mu/3) m_2 \zeta_y \\ \mu m_1 w_\zeta + (\mu/3) m_2 \zeta_z \\ \mu m_1 m_3 + (\mu/3) m_2 (\zeta_x u + \zeta_y v + \zeta_z w) \end{bmatrix} .$$

Here $m_1 = \zeta_x^2 + \zeta_y^2 + \zeta_z^2$; $m_2 = \zeta_x u_\zeta + \zeta_y v_\zeta + \zeta_z w_\zeta$; and
$m_3 = [(u^2 + v^2 + w^2)/2 + Pr^{-1}(\gamma - 1)^{-1}(a^2)]_\zeta$.

Pressure is related to the conservative flow variables Q by the equation of state

$$p = (\gamma - 1)\left[e - \frac{1}{2}\rho(u^2 + v^2 + w^2)\right] .$$

The Beam-Warming algorithm [5] is used to solve the governing equations,

$$\begin{aligned} &(I + h\delta_\xi \hat{A}^n - hD_i|_\xi)(I + h\delta_\eta \hat{B}^n - hD_i|_\eta) \\ &(I + h\delta_\zeta \hat{C}^n - hRe^{-1}\delta_\zeta J^{-1}\hat{M}^n J - hD_i|_\zeta)\Delta\hat{Q}^n \\ &\qquad = r - h(\delta_\xi \hat{E}^n + \delta_\eta \hat{F}^n + \delta_\zeta \hat{G}^n - Re^{-1}\delta_\zeta \hat{S}^n + D_e \hat{Q}^n) = \hat{R}^n , \end{aligned} \tag{2}$$

where $\hat{A}$, $\hat{B}$, $\hat{C}$, and $\hat{M}$ are the Jacobian matrices $\partial E/\partial Q$, $\partial F/\partial Q$, $\partial G/\partial Q$, and $\partial S/\partial Q$, respectively. Note that M, which is derived from S, contains

derivatives in η. For $h = (1/2)$ or 1, the integration is trapezoidal (second-order) or Euler implicit (first-order), respectively, in time. These equations are central-space-differenced and implicitly advanced in time. To maintain stability of the algorithm (because of the central-difference scheme used), an explicit fourth-order artificial-dissipation term is added to the flux calculations and an implicit second-order dissipation term is added to each of the block tridiagonals. The first working code used the above algorithm.

For steady-state computations or first-order time-integrations, a diagonal form of (2) can be used. In this case, the left and right eigenvector matrices of $\hat{A}$, $\hat{B}$, and $\hat{C}$ are used to diagonalize the one-dimensional operators. The diagonal algorithm in three dimensions has the form

$$(3) \qquad T_\xi(I + h\delta_\xi\Lambda_\xi)\hat{N}(I + h\delta_\eta\Lambda_\eta)\hat{P}(I + h\delta_\zeta\Lambda_\zeta)T_\zeta^{-1}\Delta\hat{Q}^n = \hat{R}^n \quad .$$

For a complete derivation of the diagonal algorithm (as well as definitions for $\hat{N}$, $\hat{P}$, etc.) see [28].

The main advantage of this form is the simplification of the matrix inversions from block-tridiagonal inversions to scalar-tridiagonal inversions. This simplification reduces the computational work by about 30% [28]. Also, the new scalar form for the inversion process allows the use of scalar-pentadiagonal solvers so that the added fourth-order explicit artificial dissipation can be properly linearized and be made fully implicit. This form enhances stability and convergence rates [26,29]. To further enhance the convergence rate, a space-varying Δt has been used. It is given by the formula $\Delta t = \Delta t_o/[1 + (J)^{1/2}]$, where Δt_o, as used here, is simply a constant used to decrease or increase Δt. For most cases, the default value of Δt_o

was 5. In viscous calculations the diagonal algorithm uses an explicit treatment of the viscous terms. The turbulence model used for all cases is the Baldwin-Lomax algebraic model [4].

3. Zonal approach. To initiate the zonal approach, a coarse block (zone 1) is first generated about the configuration. The coarse block can be generated either iteratively, elliptic [32], or through a marching scheme, parabolic [12]. Both procedures have the capabilities of spacing and orthogonality at the inner and outer boundaries. The topology of the grid is H-type in both the spanwise and chordwise directions.

To generate the finer zones near the wing, a small zone of points about the wing is removed from grid 1. The space left open by the removal of points from zone 1 is then occupied by the finer grid (zone 2). Zone 2 is generated by putting twice as many points in every spatial direction relative to zone 1. This task is accomplished by cubic-spline interpolation of the coarse-grid points to the fine-grid points. To generate the viscous grids, a small zone of points is again removed about the wing from zone 2. Zones 3 and 4 now occupy the area left vacant by the removal of points from zone 2. Zone 3 occupies the area above the wing and includes the upper surface of the wing, and zone 4 occupies the area below the wing and includes the lower surface of the wing. Zones 3 and 4 retain the same number of points in the streamwise and spanwise direction as does zone 2; however, points are further clustered in the normal direction to capture viscous effects. All zones overlap at the zonal boundaries, usually by one or two grid planes.

Figure 2 shows a typical grid with outer boundary positions specified so as to coincide with the position of the wind-tunnel walls from the NASA Ames High Reynolds Number Channel I [23]. The grid is plotted in perspective so

that detail on the upper and lower wind-tunnel-wall surfaces, the inflow and outflow planes, and the wing-symmetry plane are all visible. This grid, which is generated directly by the parabolic grid-generation approach, becomes the outer, coarse-grid zone (grid 1). The grid detail near the wing/symmetry-plane juncture has been removed. The blowup of the grid in this region (Fig. 3) shows the detail of the grid zones 2, 3, and 4. The wing geometry used in this case is composed of NACA 0012 cross sections, has a taper ratio of 1.0, a leading edge sweep of 20°, an aspect ratio of 3.0, and is rigged in the wind-tunnel-wall grid at an angle of attack of 2°. This wing does not have any twist or dihedral. Note that the grid immediately adjacent to the wing surface (grid zones 3 and 4) is highly clustered in the normal direction and is, therefore, appropriate for a Navier-Stokes flow solver. Also note that the Navier-Stokes grid expands in thickness from the leading edge toward the trailing edge so as to better capture the growing boundary layer.

Figure 4 illustrates the wing surface grid and a chordwise slice of zones 1, 2, and 3 at the symmetry plane ($y = 0$). Note the doubling of points in zone 2 (in chordwise and normal directions) relative to zone 1. The doubling is also done in the spanwise directions, although this is not shown here. There can also be seen a one-to-one correspondence of points in the chordwise direction (also in the spanwise direction) between zones 2 and 3, and the clustering of grid cells in zone 3. Also highlighted are the wing surface, trailing-edge mesh, and wing-tip region. Zone 4 is not shown, but it is essentially of the same structure as zone 3.

For clarification, Fig. 5 shows a generic form of the overlapping procedure between two inviscid zones (this generic overlap procedure is the same between all zones, inviscid or viscous). Boundary conditions are applied explicitly when using this overlapping procedure. That is, boundary

conditions for the zone 2, the $\xi = A$ plane, are obtained by interpolating data from the interior points of zone 1. And, conversely, boundary conditions for the zone 1, the $\xi = B$ plane, are obtained from the interior data from zone 2. The boundary conditions for a single surface are obtained with just a series of one-dimensional interpolations. The interpolation process is automated to the extent that only the two planes involved in the interpolation need to be defined, the base and target planes. Two interpolation schemes are coded: one is a cubic spline and the other is linear. The cubic spline is best in smooth regions of the flow, and the linear is best in the nonsmooth flow regions. The linear interpolation routine was used for the results presented herein. Figure 6 illustrates the possible arrangement when more zones than one are used to update the boundary conditions of zone 1. Finally in Fig. 4, zones 1 and 2 are solved using the Euler equations (inviscid zones), and the Navier-Stokes equations are used in the viscous zones (zones 3 and 4).

4. Discussion of results.

4.1. Transonic Navier-Stokes (TNS) wing-alone code. The first case tested consisted of a NACA 0012 wing, subject to the following flow conditions: $M_\infty = 0.826$, $\alpha = 2°$, and a Reynolds number, based on the chord, of 8 million. This case, which is moderately difficult, involves a strong shock that extends from zone 3 (viscous upper-surface zone) into zones 2 and 1 (inviscid zones). With the zonal approach, the test case was run on a 150,000-point mesh, which for three dimensions is a relatively fine grid.

For this case the wind-tunnel-wall effects are very significant. This effect can be seen in Fig. 7 where the pressure coefficient distributions from the TNS code, with and without the walls modeled, are compared with those of

experiment [23]. The shift in shock position caused by the tunnel walls is obvious. The shock position for the case with walls is in good agreement with the experimental shock position.

General agreement between the wind-tunnel-wall case and experiment is better inboard of mid-semispan than it is outboard. In particular, the computed upper-surface shock strength at $2y/b = 0.78$ is larger than that of the experiment. This larger strength is caused by a large boundary-layer separation in the experimental results at this semispan location, which is not accurately reproduced by the computed results. A good picture of this situation is given in Figs. 8 and 9, which show a set of computed particle paths (Fig. 8) and an oil-flow photograph taken from the experiment (Fig. 9). The experimental separation is about twice as large as the computed separation. The spanwise extent of the experimental separation is reasonably predicted by the computation, but the streamwise extent is underpredicted. Some reasons for this discrepancy are coarse-grid and turbulent-model effects, as well as the sensitivity of the flow pattern to changes in the free-stream Mach number. Despite the difference in the size of the separation zone, the overall comparison is quite encouraging.

Figure 10 shows Mach number contours plotted in a wing cross-sectional plane at a semispan station of $2y/b = 0.66$; the zonal boundaries are highlighted. Note the smoothness with which the shock wave crosses the zonal interface boundary. This demonstrates that this particular interface, between zones 2 and 3, is implemented in a conservative manner. (It should be noted, however, that not all interfaces are conservative.) Generally, most of the other contours cross the zonal interface boundaries in a smooth and continuous way. Downstream in the wake where the fine viscous grid interfaces with a relatively coarse inviscid grid (see Fig. 3), the wake abruptly stops. This

is due to the difference in grid refinement (in going from the wing grid to the fine, but not clustered, grid 2). The power of the zonal scheme allows the addition of more zones in those regions where large gradient flow is observed. In the wing-fuselage case, a special zone is implemented downstream of the wing to capture the important viscous wake effects.

The convergence rate of the diagonal version versus the block ADI version is illustrated in Fig. 11. The time-step used in the nondiagonal version was $\Delta t = 0.004$, which was the largest time-step possible while still maintaining stability of the code. The diagonal version used a variable time-step (as described previously). Even though the comparison is between a fixed time-step solution and a variable time-step solution, the main speedup in the diagonal algorithm is not in the variable time-stepping procedure, but in the proper linearization of the dissipation terms [26]. The slow rate of convergence in the nondiagonal version seems to occur in the outer inviscid zones. The residual in the viscous zones in the first thousand iterations drops fairly fast, then begins to flatten out. In 5,000 iterations, all zones have dropped about two orders of magnitude in the L2 norm of the residual. In contrast, the convergence rate of the diagonal version drops rapidly in all the zones. A three-order-of-magnitude drop in the L2 norm occurs in about 400-500 iterations. This convergence rate (coupled with the decrease in arithmetic operation count caused by the diagonal algorithm) increases the speed with which solutions are obtained by a factor of 40. The faster convergence rate, as stated before, is due to the proper linearization of the fourth-order-explicit dissipation operator. This rate was possible in the nondiagonal version, but would involve inverting block pentadiagonals, which would substantially increase the computational cost. More time was required

for the same case when wind-tunnel walls were modeled, since a stronger shock occurs.

We can also look at the development of lift and the number of supersonic points (NSP) to study the convergence characteristics. Figure 12 shows the evolution where the x-axis is the number of iterations; the y-axis is left unlabeled (since the actual values were not of significance, but the overall trend in the approach to the steady state is important). The NSP overshoots the final converged solutions at about 100 iterations, but then quickly approaches the converged solution. At about 200 iterations, it is within 7% of the converged solution, and at 300 iterations it is within 1%. The lift also overshoots the final converged value, but at 200 iterations it is within about 4% of the final solution, and at 300 iterations it is within 1%. If, instead of a three-order-of-magnitude drop in residual, convergence is based on 95% of the converged lift, then a solution can be generated in about 200 iterations, or about 18 min of cpu time for this fine-grid calculation.

The next case presented consists of a massive, shock-induced, boundary-layer separation. This case was computed to ascertain the degree of robustness of the present algorithm and, in particular, the ability of the present zonal interface scheme to cope with large flow gradients. The geometry used is the same as that of the last case. The free-stream Mach number and angle of attack have been arbitrarily chosen to be 0.9 and 5°, respectively. Utilization of the wind-tunnel-wall boundaries produced a "choked" solution with a shock wave spanning the tunnel. After several hundred iterations and a moderately converged calculation, the solution diverged as expected. This result was a consequence of the "fixed" upstream boundary conditions forcing more mass flow through the tunnel than the choked condition would allow.

The solution was repeated with free-air boundary conditions, and then convergence was easily achieved. Computed particle paths on the upper wing surface are displayed in Fig. 13. Note that approximately half of the upper wing surface is separated. The solution contains several interesting features, including a separation saddle point, a focus, a reattachment saddle point, and a node. Note also that this computed solution has a stable sequence of critical points on the separation line; that is, a node followed by a saddle point and then a focus. This case required about 2.8 hr of cpu time.

Two different perspective views of the three-dimensional particle paths are shown in Fig. 14. Figure 14a shows a view from outboard of the wingtip, and Fig. 14b shows a view from behind and above the wing. The height and three dimensionality of the separation zone are apparent in these figures. The dashed particle paths move along the wing surface until the separation line is encountered; then they are deflected up and over the separation bubble, with a few of the dashed paths captured by the primary swirling flow at the center of the wing. The solid particle paths are more intimately involved with the two swirling pockets of flow, and they essentially define these regions.

The position of the separation region relative to the zonal interface boundary is best displayed by plotting particle paths constrained to lie in spanwise cross-sectional planes. Two such plots are displayed in Fig. 15. Figure 15a shows cross-sectional particle paths for a semispan station of $2y/b = 0.66$. The separation region is large and easily extends above the zonal boundary from the Navier-Stokes region into the Euler region. Nevertheless, the solution looks qualitatively reasonable. An enlargement of the separated portion of the solution is shown in Fig. 15b. From this figure it

can be seen that the particle paths pass smoothly across the interface boundary with no function or slope discontinuities. Thus, the primary objective of doing this calculation was achieved. Despite the existence of a strong shear gradient across the explicitly updated interface boundary, the present approach is capable of predicting a stable solution that is reasonably free from interface boundary influence.

Figure 16 shows Mach number contours for this difficult transonic case at a semispan station of $2y/b = 0.33$. A very strong shock can be seen on the upper surface of the wing, as well as its smooth transition to the other zones. The wake region is larger because of the shock induced separation region.

For more details on the zonal procedure, convergence studies, transonic results with different wings, and data management structure, the reader is referred to [13,19,20].

The zonal grid topology described in the previous section utilizes Cartesian-like grids to simplify the zonal interfacing and to maintain flow conservation at shocks. One drawback to this approach, however, is the resulting Hd-mesh singularity at the wing leading edge. This occurs at the interface between blocks 3 and 4, as shown in Fig. 17. It is important to be able to properly treat severe coordinate singularities because they naturally arise in realistic aircraft configurations.

Some of the early computations with the TNS code were performed at low to moderate angles of attack and used simple central differencing of the metrics. For these relatively simple test cases, there appeared to be no difficulty at the wing leading edge. In order to control metric truncation errors and insure uniform flow as an exact solution of the finite-difference equations, the free-stream residual was subtracted from the right side of (1).

However, for $M_\infty = 0.5$ and $\alpha = 10°$, large oscillations in the flow variables developed at the H-mesh singularity, as indicated by the wing root section Mach number contours given in Fig. 18. It was not possible to obtain a fully converged solution. A nominal two-order-of-magnitude drop in the L_2 norm of the residual was possible only after adding large amounts of numerical dissipation near the leading edge. This was clarly unacceptable and would prevent high-angle-of-attack simulations. This problem was fixed by using free-stream preserving metrics as described by Pulliam and Steger [27].

In their work, Pulliam and Steger used special numerical metrics that insured uniform flow was: (1) an exact solution of the finite-difference equation; or (2) the free-stream subtraction described above. In the cases treated in [27], Pulliam and Steger found no appreciable difference between the two solutions or in their convergence rates, and therefore preferred the latter approach. However, their grids were relatively smooth and did not possess severe coordinate singularities such as are present in the H-type. Once the free-stream preserving metrics were implemented in the TNS code, there was no difficulty in rapidly converging to a steady state, and no additional dissipation was necessary at the leading edge. (For more details into the theory of the free-stream preserving metrics, see [7].) The resulting, improved, Mach-number contours are shown in Figs. 19 and 20. There is a nominal amount of distortion at the interface of blocks 3 and 4 because the flow variables are obtained there using simple averages instead of from the governing equations. The L_2 norm of the residuals for all four blocks are shown in Fig. 21. A three-order-of-magnitude drop in the residuals of all four blocks was obtained in 700 iterations. This criterion for convergence is usually sufficient for plottable accuracy.

The first set of solutions was obtained at a free-stream Mach number $M_\infty = 0.5$. A comparison between TNS lift and drag coefficients and those obtained with a method based on the full-potential equations [18] is shown in Figs. 22 and 23. Unfortunately, good-quality force, moment, and surface-pressure data, up through maximum lift, are lacking in the literature. Although force and moment data provide a way to assess a code's global accuracy, extensive surface-pressure data are necessary for validating the details of the flow simulation. These flow simulations indicate that the flow is subcritical owing to the effects of three-dimensional relief and wing sweep. Sonic flow is achieved only at maximum lift ($\alpha = 13.5°$). The lift coefficient obtained with the TNS code is in good agreement with the full-potential result in the low-angle-of-attack range, but differs significantly in the high-angle-of-attack range. The TNS code predicts maximum lift at $\alpha = 13.5°$, whereas the full-potential lift coefficient continues in a linear fashion. The drag coefficient exhibits the usual quadratic variation with angle of attack ($C_D \sim C_L^2 \sim \alpha^2$) together with the large drag rise at stall. A converged solution usually requires 700 iterations, or 55 min of Cray X-MP time.

Particle trajectories for $\alpha = 15°$ are shown in Figs. 24 and 25. Figure 24 is a perspective view from above the wing and looking downstream toward the wing leading edge. The particles are released along the wing leading edge and wing tip. This massively separated steady flow exhibits α-induced separation, that is, separation caused solely by angle of attack, as apposed to shock-induced separation. The vortical structure of the separated region is evident. The particle trajectories emanating from the wing tip indicate a wing-tip vortex. Figure 25 is an end view of the wing looking inboard from the wing tip. The region of separation extends across zonal boundaries in a smooth manner. This solution seems to be on the verge of

going unsteady, and it required twice as many iterations to achieve convergence. The spatially varying time-step tends to inhibit unsteadiness. When a constant time-step was used, a cyclic variation in the residuals was noted.

All of these solutions were obtained with little difficulty, provided consistent metrics were used. Without these special free-stream-preserving metrics, solutions at angles of attack greater than 5° would not converge. These high-angle-of-attack solutions also demonstrate the robustness of the zonal approach.

Transonic wing solutions were also obtained for $M_\infty = 0.8$. The TNS C_L vs α vaiation is compared with the previous subcritical case in Fig. 26. In this transonic flow, maximum lift occurs at a much lower angle of attack ($\alpha = 6°$), a result of shock-induced separation. These transonic solutions were relatively easy to obtain, requiring 50 min per solution.

The wing-tip vortex for the maximum lift condition, $\alpha = 6°$, is shown in Fig. 27. A very interesting simulated oil-flow pattern on the upper surface of the wing is shown in Fig. 28. These are particle trajectories constrained to the next coordinate surface above the wing (because of the no-slip condition on the wing). Notice the saddle and nodal point singularities on the upper surface of the wing. These critical points form a stable topological configuration as defined in [34]. There is a major separation line extending over most of the wing span, and it is followed by a reattachment line (shown by a dashed line) a short distance downstream. A second small separation region is also evident near the trailing edge in the vicinity of the wing tip.

The extent of separation in these subcritical and transonic cases tends to be underpredicted. This was also evident for the initial test case in which comparisons were made between simulated and experimental surface oil-flow patterns. There are several reasons for this discrepancy. First, better

grid resolution is probably required to improve the accuracy of the computation. Grid-refinement studies using a million-point wing grid on the Ames Cray 2 are in progress. Second, an improved numerical dissipation model is required. Blended fourth-order and second-order smoothing is used in (1) as described by Pulliam [26]. This blended smoothing has very good shock-capturing chearacteristics on a grid suitable for the Euler equations. However, the dissipation coefficient varies as $O(1/\Delta z)$ and, on fine-spaced grids needed for viscous computations the numerical dissipation can be as large as the physical dissipation. Finally, an improved and efficient turbulence model is required that can adequately model three-dimensional shock-induced separation. The first two points will be easily achievable in the near future, but the latter still remains uncertain.

4.2 TNS wing-fuselage code. As previously mentioned, one of the advantages of the zonal method is the ability to create grids, about complicated aircraft, with sufficient clustering of points on all no-slip surfaces. Figure 29 shows body-conforming zonal grids of a fighter aircraft configuration in the physical and computational spaces. Figure 30 illustrates the base grid that is used by the zoner code to create the different zones about this modified F-16A aircraft. This grid was generated via an elliptic grid-generating technique [32]. From this figure the polar type of topology about the fuselage can be seen. This polar grid collapses into a singular line in front of the fuselage nose but, because of the averaging about this singularity, there is no problem in the flow solver. A chordwise slice through the wing would reveal an H-mesh-type of local topology. The modified F-16A can be seen in Fig. 31, illustrating the exclusion of the tail assembly. From Figs. 31a and 31b, it can be noted that the forebody, canopy, leading-edge

strake, wing, and shelf regions are unmodified and are of the exact geometry of the F-16A. The inlet is faired over. Figure 32 shows a planform view of the base grid. Generating even a base grid with no clustering normal to the surfaces is difficult. Because of the tapering of the wing (the horizontal tail is not computed here), the grid lines tend to squeeze together at the leading edge near the tip region, then suddenly stretch out as they continue to the outer boundary.

The base grid is fed into a zonal routine, which then subsequently creates 16 zones (by subdividing the original base grid). Through certain parameters in the zonal routine, the zones created are essentially of three types: (i) inviscid zones, (ii) viscous zones with clustering on one face of the zone for wing or fuselage surfaces, and (iii) viscous zones with clustering on two adjacent faces of the zone for the wing-fuselage juncture. Figure 33 shows a schematic view of the 18 zones created for the F-16A. Zones 1 and 4 are on the fuselage and are constructed with sufficient grid resolution in the normal direction. Zones 8 and 9 (zone 9 is not visible) are on the upper and lower wing, respectively, and also have sufficient grid clustering. Zones 2 and 3 (zone 3 is not visible) are special, in that they have clustering both normal to the wing and normal to the fuselage surfaces. This is in order to capture viscous effects caused by the wing-fuselage juncture. Zones 12 and 13 are not considered to be no-slip surfaces; however, they are clustered across the wing planform plane, in order to capture wake (zone 12) and tip (zone 13) effects. Zone 6 is also clustered both normal to the fuselage and across the wing planform plane. (Viscous effects and appropriate turbulence model effects are implemented for these zones and solved with the thin-layer Navier-Stokes equations. All other zones are solved with

the Euler equations.) Results will be shown only for a 16-zone version of the modified F-16A.

Figure 34 shows some of the different wing-fuselage mesh topologies. The topology chosen was that of Fig. 34a. It allowed for clustering in the wing-fuselage juinction, and made it easier to implement the turbulence model. Figure 35 shows the clustering in the viscous zones. The viscous zone is based on the first three inviscid points of the body, NJC = 1-3. Then a single parameter, per block, determines the amount of clustering to be implemented. A different interpolation routine from that of the wing-alone code is required. Instead of simple one-dimensional interpolation [19], two-dimensional interpolation is now required because of the interfacing of surfaces. This can be seen in Fig. 36, where surface ABCD from a coarse zone, may be used to interpolate the surface onto a fine grid.

Pressure contours are displayed in Fig. 37 for flow conditions of $M_\infty = 0.9$, $\alpha = 1.69°$, and a Reynolds number based on the chord of 4.5 million. The coalescing of contours indicates regions of high gradient flow. Stagnation flow occurs at the fuselage nose and at the forward base of the canopy. The flow then accelerates over the top of the canopy. At the leading edge of the wing, the flow accelerates and smoothly decelerates as it approaches the trailing edge. Notice how the pressure contours continue from the upper wing zone into the fuselage zone. Similarly, the fuselage has two zones, the boundary occurring approximately at the base of the back of the canopy. Pressure contours continue smoothly between these two zones.

Mach contours are plotted in Fig. 38. These contours were calculated on planes that were about 15 grid points up from the surfaces, so as to be out of the boundary-layer region. The peak Mach number is about 1.2, and the contours on the wing indicate a weak shock, if any, occurring.

These calculations required about 2,500 iterations on a total grid size of about 300,000 points. This required about 10 hr of cpu time on the Cray X-MP-48. For results from other transonic calculations, as well as at higher angles of attack, the reader is referred to [14,31].

5. Conclusions. A fast diagonal algorithm has been successfully implemented within the framework of a zonal approach. Results indicate that the modified code (in obtaining a solution for a moderately difficult case) still maintains its fast convergence characteristics. This improvement is demonstrated by producing a three-dimensional, fine-grid Euler/Navier-Stokes wing solution in 45 min on the Cray X-MP, which is faster by a factor of 40 than the original code. Computed pressures and oil-flow patterns compare favorably with those of experiment. The wing code has been extended to a 16-block version for the modified F-16A geometry. The zonal procedure allows appropriate grid clustering normal to all no-slip surfaces, and pressure contours continue smoothly across the different zones. The calculations require about 10 hr of cpu time for 300,000 grid points.

REFERENCES

[1] E. H. ATTA, Component-adaptive grid interfacing, AIAA Paper 81-0382, Orlando, Fla., 1982.

[2] E. H. ATTA AND J. A. VADYAK, Grid interfacing zonal algorithm for three-dimensional transonic flows about aircraft configurations, AIAA Paper 82-1017, 1982.

[3] T. J. BAKER, A. JAMESON, AND R. E. VERMELAND, Three-dimensional Euler solutions with grid embedding, AIAA Paper 85-0121, Reno, Nev., 1985.

[4] B. S. BALDWIN AND H. LOMAX, Thin-layer approximation and algebraic model for separated turbulent flows, AIAA Paper 78-257, 1978.

[5] R. M. BEAM AND R. F. WARMING, An implicit finite-difference algorithm for hyperbolic systems in conservation law form, J. Comp. Phys. 22(1976), pp. 87-110.

[6] L. CAMBIER, W. GHAZZI, J. P. VEUILLOT, AND H. VIVIAND, Une approache par domaines pour le calcul d'ecoulements compressibles, Cinquieme Colloque International sur les Methodes de Calcul Scientifique et Technique, INRIA, Versailles, France, December 1981.

[7] N. M. CHADERJIAN, Transonic Navier-Stokes wing solutions using a zonal approach Part 2: High angle-of-attack simulation, 58th Meeting of the Fluid Dynamics Panel Symposium on Applications of Computational Fluid Dynamics in Aeronautics, Aix-en-Provence, France, April 1986.

[8] N. M. CHADERJIAN AND J. L. STEGER, A zonal approach for the steady transonic simulation of inviscid rotational flow, AIAA Paper 82-1927, 1983.

[9] G. S. DEIWERT AND H. ROTHMUND, Three-dimensional flow over a conical afterbody containing a centered propulsive jet: A numerical simulation, AIAA Paper 83-1709, 1983.

[10] G. S. DEIWERT, A. E. ANDREWS, AND K. NAKAHASHI, Theoretical analysis of aircraft afterbody flow, AIAA Paper 84-1524, 1984.

[11] L. ERIKSSON, Euler solutions on O-O grids around wings using local refinement, 6th GAMM Conference on Numerical Methods in Fluid Mechanics, Göttingen, West Germany, 1985.

[12] T. A. EDWARDS, Noniterative three-dimensional grid generation using parabolic partial differential equations, AIAA Paper 85-0485, 1985.

[13] J. FLORES, Convergence acceleration for a three-dimensional Euler/Navier-Stokes zonal approach, AIAA Paper 85-1495, 1985.

[14] J. FLORES, S. G. REZNICK, T. L. HOLST, AND K. GUNDY, Navier-Stokes solutions for a fighter-like configuration, AIAA Paper 87-0032, Reno, Nev., 1987.

[15] K. FUJII AND P. KUTLER, Numerical simulation of the viscous flow fields over three-dimensional complicated geometries, AIAA Paper 83-1098, Reno, Nev., 1983.

[16] K. A. HESSENIUS AND T. H. PULLIAM, Azonal approach to solution of the Euler equations, AIAA Paper 82-0969, 1984.

[17] K. A. HESSENIUS AND M. M. RAI, Three-dimensional, conservative, Euler computations using patched grid systems and explicit methods, AIAA Paper 86-1081, 1986.

[18] T. L. HOLST AND S. D. THOMAS, Numerical solution of transonic wing flow fields, AIAA Paper 82-0105, 1982.

[19] T. L. HOLST, U. KAYNAK, K. L. GUNDY, S. D. THOMAS, J. FLORES, AND N. M. CHADERJIAN, Numerical solution of transonic wing flows using an Euler/Navier-Stokes zonal approach, AIAA Paper 85-1640, 1985.

[20] T. L. HOLST, S. D. THOMAS, U. KAYNAK, K. L. GUNDY, J. FLORES, AND N. M. CHADERJIAN, Computational aspects of zonal algorithms for solving the compressible Navier-Stokes equations in three dimensions, NASA TM-86774, 1985.

[21] S. J. KLINE, B. J. CANTWELL, AND G. M. LILLEY, EDS., Proceedings, 1980-1981 AFOSR-HTTM-Stanford Conference on Complex Turbulent Flows, Stanford University, Stanford, Calif., 1982.

[22] K. D. LEE, M. HUANG, N. J. YU, AND P. E. RUBBERT, Grid generation for three-dimensional configurations, NASA CP-2166, 1980.

[23] W. K. LOCKMAN AND H. L. SEEGMILLER, An experimental investigation of the subcritical and supercritical flow about a swept semispan wing, NASA TM-84367, 1983.

[24] N. N. MANSOUR, Numerical simulation of the tip vortex off a low-aspect wing at transonic speed, AIAA Paper 84-0522, 1984.

[25] L. PRANDTL, Uber Flussigkeitsbewegung bei sehr kleiner Reibung, AIAA Paper 81-0382, Orlando, Fla., 1982.

[26] T. H. PULLIAM, Artificial dissipation models for the Euler equations, AIAA Paper 85-0438, 1985.

[27] T. H. PULLIAM AND J. L. STEGER, Implicit finite-difference simulation of three-dimensional compressible flow, AIAA J. 18(1980), pp. 159-167.

[28] T. H. PULLIAM AND D. S. CHAUSSEE, A diagonal form of an implicit approximate-factorization algorithm, J. Comp. Phys. 39(1981), pp. 347-363.

[29] T. H. PULLIAM AND J. L. STEGER, Recent improvements in efficiency, accuracy, and convergence for implicit approximate-factorization algorithms, AIAA Paper 85-0360, Reno, Nev., 1985.

[30] M. M. RAI, A conservative treatment of zonal boundaries for Euler calculations, AIAA Paper 84-0164, 1984.

[31] S. G. REZNICK AND J. FLORES, Strake-generated vortex interactions for a fighter-like configuration, AIAA Paper 87-589, Reno, Nev., 1987.

[32] R. L. SORENSON, Three-dimensional elliptic grid generation about fighter aircraft for finite-difference solutions, to be published as a NASA Technical Memorandum.

[33] J. L. STEGER, F. C. DOUGHERTY, AND J. A. BENEK, A chimera grid scheme, Mini-Symposium on Advances in Grid Generation, ASME Applied Bioengineering and Fluids Engineering Conference, Houston, Tex., 1983.

[34] M. TOBAK AND D. J. PEAKE, Topological structures of three-dimensional separated flows, AIAA Paper 81-1260, 1981.

[35] N. J. YU, Transonic flow simulation for complex configurations with surface fitted grids, AIAA Paper 81-1258, St. Louis, Mo., 1981.

FIGURE CAPTIONS

FIG. 1. Zonal interface alternatives.

FIG. 2. Global finite-difference grid showing wing-tunnel walls.

FIG. 3. Expanded view of embedded grid near wing.

FIG. 4. Perspective view of embedded grid with upper symmetry plane ($y = 0.0$) and wing surface highlighted: $\lambda_{LE} = 20°$, AR = 3.0, TR = 1.0.

FIG. 5. Grid zone interface procedure: (a) two-zone grid arrangement showing overlap, (b) grid point detail in the overlap region (ξ = A plane).

FIG. 6. Overlap between zones 2 and 3 removed for clarity.

FIG. 7. Pressure coefficient comparisons: NACA 0012 airfoil section, AR = 3.0, $\Lambda_{LE} = 20°$, TR = 1.0, $M_\infty = 0.826$, $\alpha = 2°$, $R_e = 8 \times 10^6$.

FIG. 8. Computed particle paths on the upper wing surface: NACA 0012 airfoil section, AR = 3.0, $\Lambda_{LE} = 20°$, TR = 1.0, $M_\infty = 0.826$, $\alpha = 2°$, $R_e = 8 \times 10^6$.

FIG. 9. Oil-flow pattern on upper wing surface: NACA 0012 airfoil section, AR = 3.0, $\Lambda_{LE} = 20°$, TR = 1.0, $M_\infty = 0.826$, $\alpha = 2°$, $R_e = 8 \times 10^6$ (from [23]).

FIG. 10. Cross-sectional Mach-number contours: NACA 0012 airfoil section, AR = 3.0, $\Lambda_{LE} = 20°$, TR = 1.0, $M_\infty = 0.826$, $\alpha = 2°$, $R_e = 8 \times 10^6$.

FIG. 11. Convergence rate comparison.

FIG. 12. Development of lift and number of supersonic points (NSP).

FIG. 13. Computed particle paths on the upper wing surface: NACA 0012 airfoil section, AR = 3.0, $\Lambda_{LE} = 20°$, TR = 1.0, $M_\infty = 0.9$, $\alpha = 5°$, $R_e = 8 \times 10^6$.

FIG. 14. Computed three-dimensional particle paths on the upper wing surface: NACA 0012 airfoil section, AR = 3.0, Λ_{LE} = 20°, TR = 1.0, M_∞ = 0.9, α = 5°, R_e = 8 × 10^6: (a) view from behind and above wing; (b) view from outboard of wing tip.

FIG. 15. Copmputed cross-sectional particle paths: NACA 0012 airfoil section, AR = 3.0, Λ_{LE} = 20°, TR = 1.0, M_∞ = 0.9, α = 5°, R_e = 8 × 10^6: (a) 2y/b = 0.66; (b) 2y/b = 0.66, expanded view of separated flow region.

FIG. 16. Cross-sectional Mach-number contours: NACA 0012 airfoil section, AR = 3.0, Λ_{LE} = 20°, TR = 1.0, M_∞ = 0.9, α = 5°, R_e = 8 × 10^6.

FIG. 17. H-mesh singularity at wing leading edge (blocks 3 and 4): NACA 0012, M_∞ = 0.5, α = 10.0°, R_e = 8 × 10^6.

FIG. 18. Symmetry plane Mach-number contours with central-difference metrics: NACA 0012, M_∞ = 0.5, α = 10.0°, R_e = 8 × 10^6.

FIG. 19. Symmetry plane Mach-number contours with new metrics: NACA 0012, M_∞ = 0.5, α = 10.0°, R_e = 8 × 10^6.

FIG. 20. Symmetry plane Mach-number contours with new metrics: NACA 0012, M_∞ = 0.5, α = 10.0°, R_e = 8 × 10^6.

FIG. 21. L_2 norm convergence history of residuals for all four blocks: M_∞ = 0.5, α = 10.0°, R_e = 8 × 10^6.

FIG. 22. Lift coefficient comparison between TNS and full-potential code: NACA 0012, M_∞ = 0.5, R_e = 8 × 10^6.

FIG. 23. Drag coefficient comparison between TNS and full-potential code: NACA 0012, M_∞ = 0.5, R_e = 8 × 10^6.

FIG. 24. Perspective view of particle trajectories over a stalled wing: NACA 0012, M_∞ = 0.5, α = 15.0°, R_e = 8 × 10^6 (view from above the wing, looking downstream toward the wing leading edge).

FIG. 25. Particle trajectories over a stalled wing (view looking inboard from wing tip): NACA 0012, $M_\infty = 0.5$, $\alpha = 15.0°$, $R_e = 8 \times 10^6$.

FIG. 26. TNS lift coefficient comparison between subcritical ($M_\infty = 0.5$) and transonic ($M_\infty = 0.8$) cases: NACA 0012.

FIG. 27. Particle trajectories of the wing-tip vortex at maximum lift: NACA 0012, $M_\infty = 0.8$, $\alpha = 6.0°$, $R_e = 8 \times 10^6$; the wing planform near the wing tip is shaded.

FIG. 28. Numerical oil-flow pattern on upper wing surface: NACA 0012, $M_\infty = 0.8$, $\alpha = 6.0°$, $R_e = 8 \times 10^6$ (N-node critical point, S-saddle critical point).

FIG. 29. Body-conforming zonal grids of a fighter aircraft configuration in the physical and computational spaces.

FIG. 30. Base grid generated by an elliptic method: $60 \times 20 \times 24$ grid points.

FIG. 31. View of surface grid for the modified F-16A: (a) view from above; (b) view from side.

FIG. 32. Planform view of the base grid.

FIG. 33. A schematic view of the zonal structure for the modified F-16A.

FIG. 34. Different wing-fuselage mesh topologies: (a) polar topology; (b) H-topology.

FIG. 35. Grid clustering normal to no-slip surfaces: (a) coarse grid; (b) refined viscous grid.

FIG. 36. Fine-coarse zone interface: (a) two-zone grid showing overlap at ABCD and EFGH planes in physical space; (b) grid point detail in the overlap region in transformed space.

FIG. 37. Pressure contours: $M_\infty = 0.9$, $\alpha = 1.69°$, $R_e = 4.5 \times 10^6$.

FIG. 38. Mach contours: $M_\infty = 0.9$, $\alpha = 1.69°$, $R_e = 4.5 \times 10^6$.

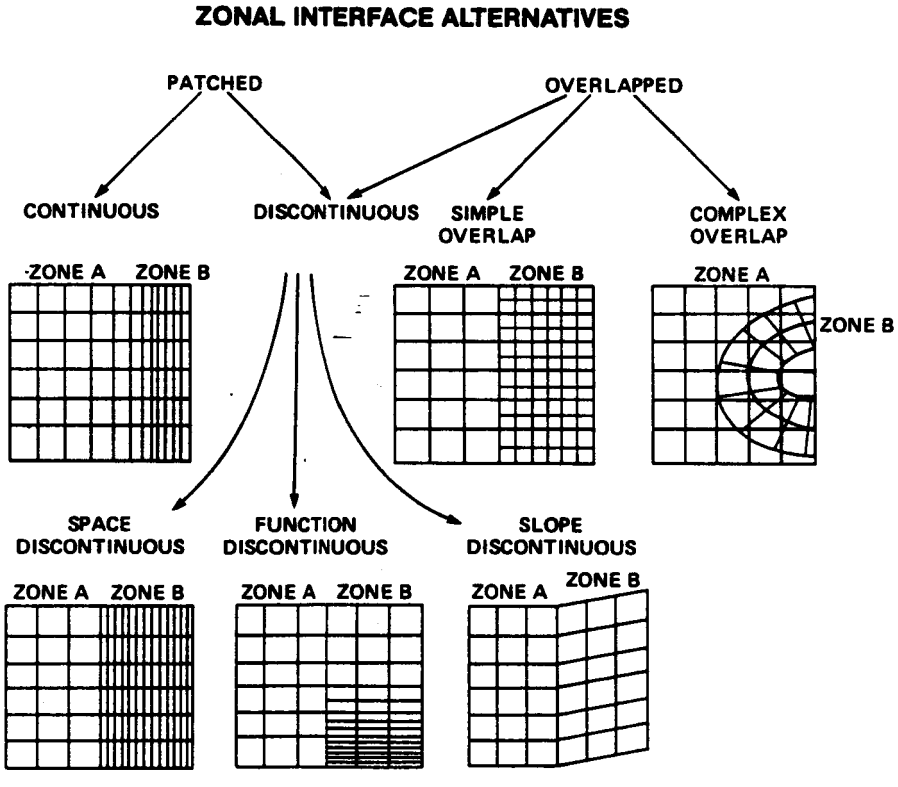
ZONAL INTERFACE ALTERNATIVES
PATCHED
OVERLAPPED
CONTINUOUS
DISCONTINUOUS
SIMPLE OVERLAP
COMPLEX OVERLAP
ZONE A
ZONE B
ZONE A
ZONE B
ZONE A
ZONE B
SPACE DISCONTINUOUS
FUNCTION DISCONTINUOUS
SLOPE DISCONTINUOUS
ZONE A
ZONE B
ZONE A
ZONE B
ZONE A
ZONE B

Fig. 1

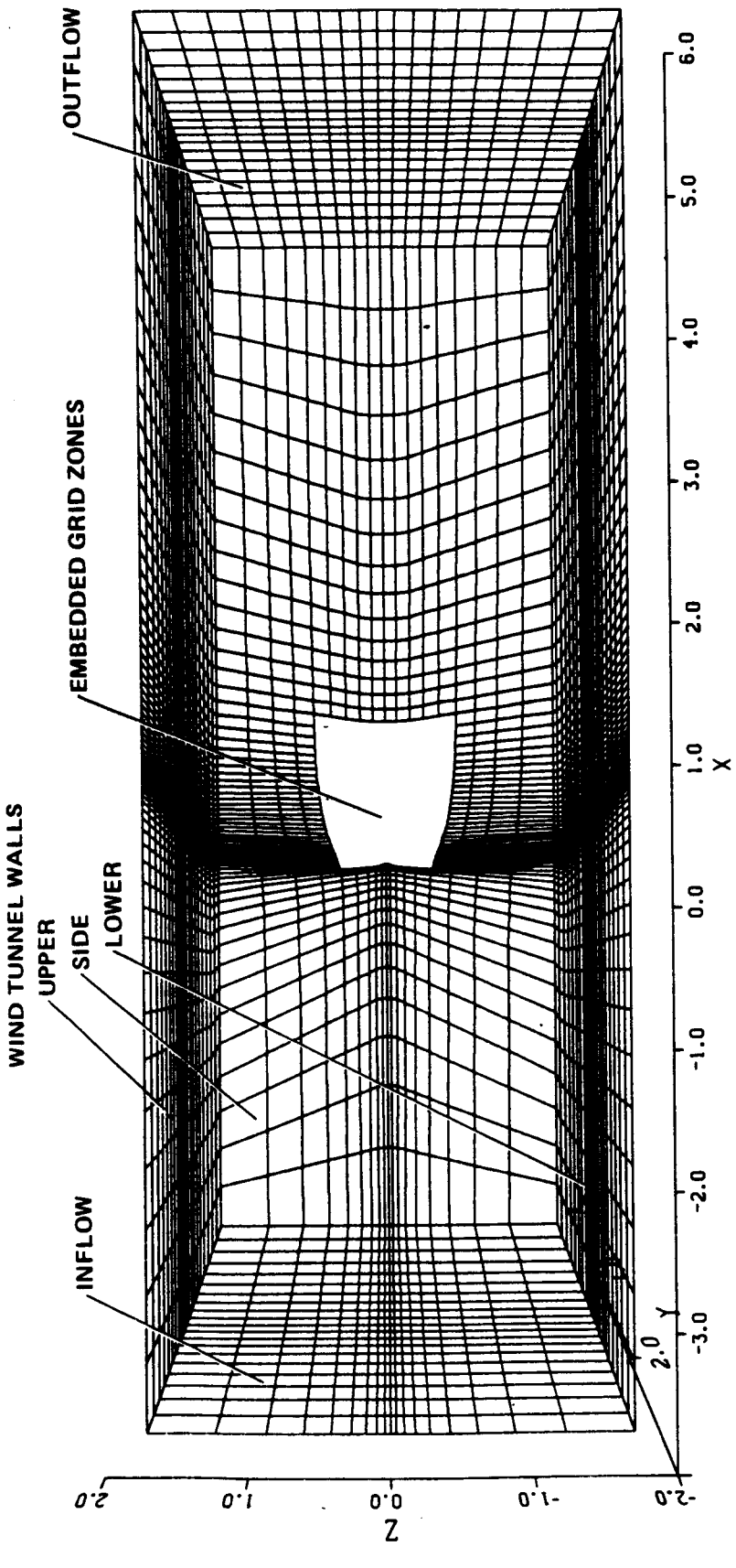
OUTFLOW
EMBEDDED GRID ZONES
WIND TUNNEL WALLS
UPPER
SIDE
LOWER
INFLOW
Z
2.0
1.0
0.0
-1.0
-2.0
X
6.0
5.0
4.0
3.0
2.0
1.0
0.0
-1.0
-2.0
-3.0
Y
2.0

Fig. 2

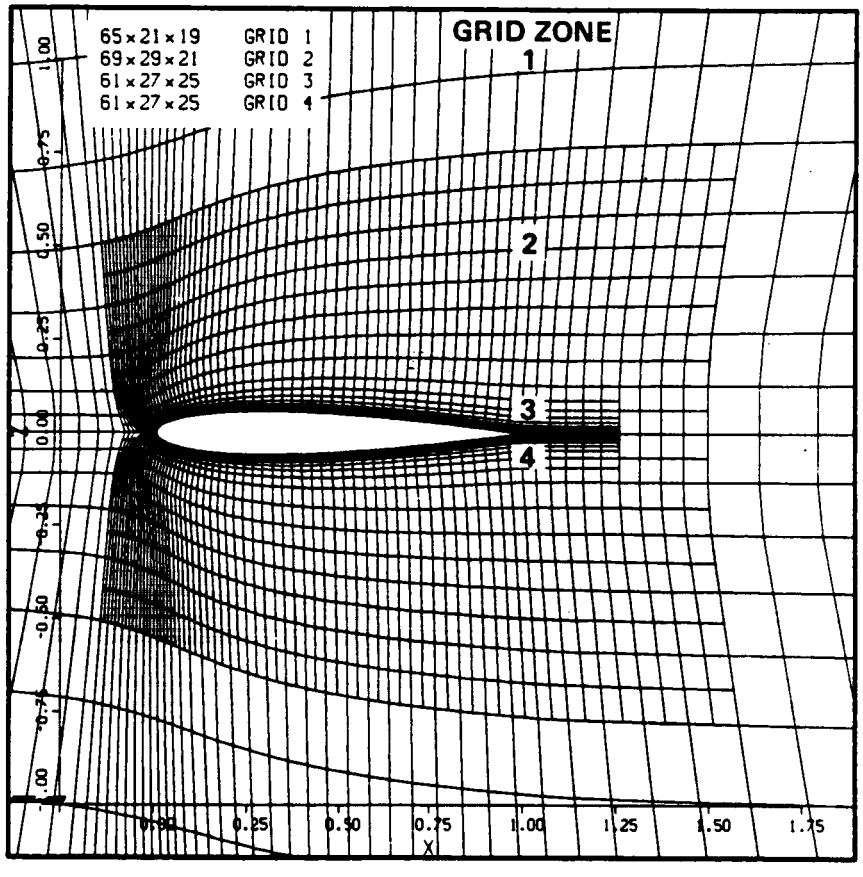

Fig. 3

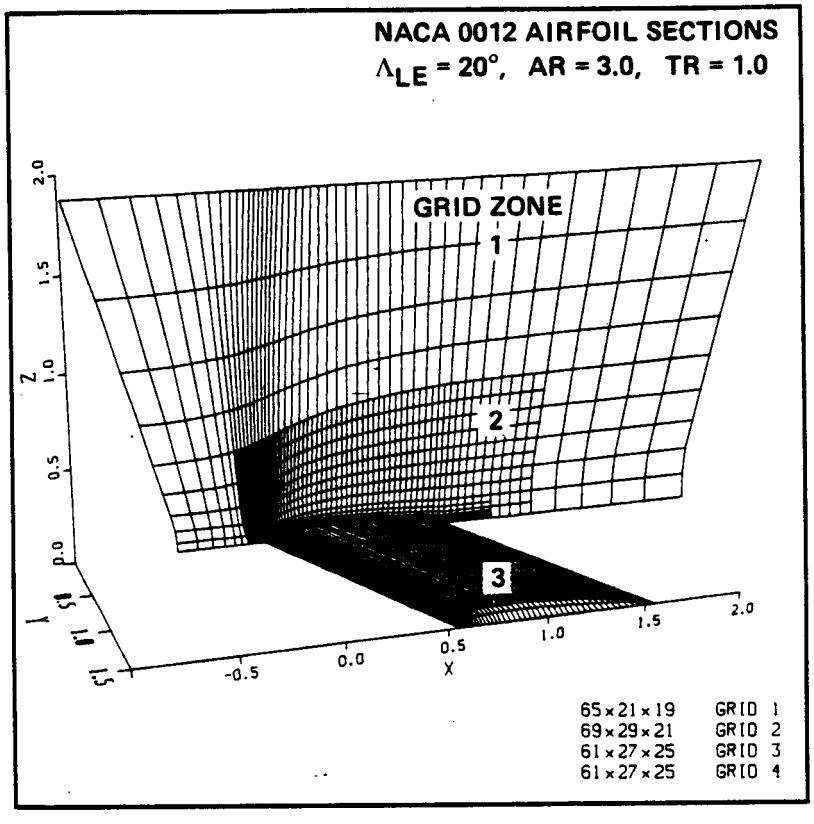
NACA 0012 AIRFOIL SECTIONS
Λ_{LE} = 20°, AR = 3.0, TR = 1.0
GRID ZONE
1
2
3
Z
X
2.0
1.5
1.0
0.5
0.0
-0.5
65×21×19 GRID 1
69×29×21 GRID 2
61×27×25 GRID 3
61×27×25 GRID 4

Fig. 4

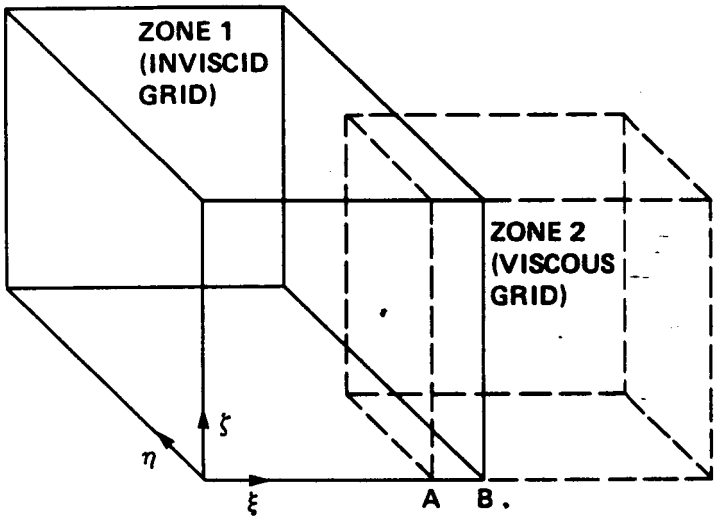

a) TWO-ZONE GRID ARRANGMENT SHOWING OVERLAP

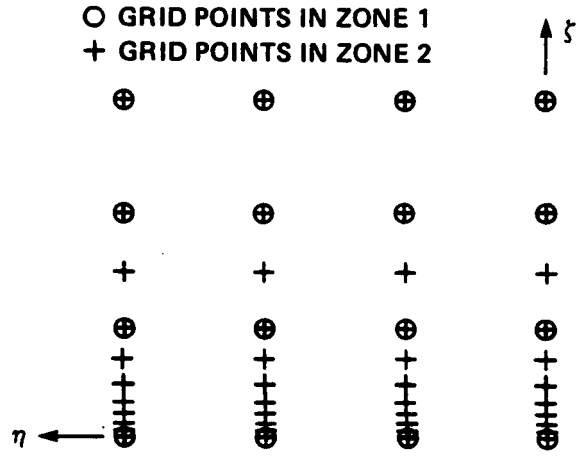

b) GRID POINT DETAIL IN THE OVERLAP REGION (ξ = A PLANE)

Fig. 5

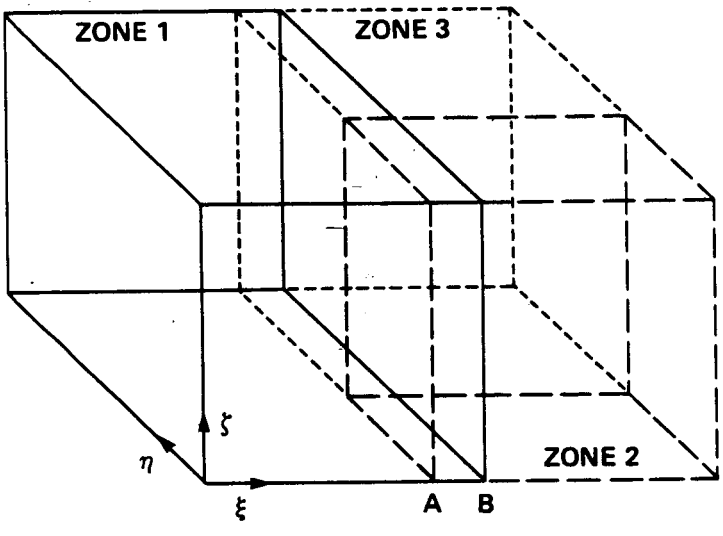

Fig. 6

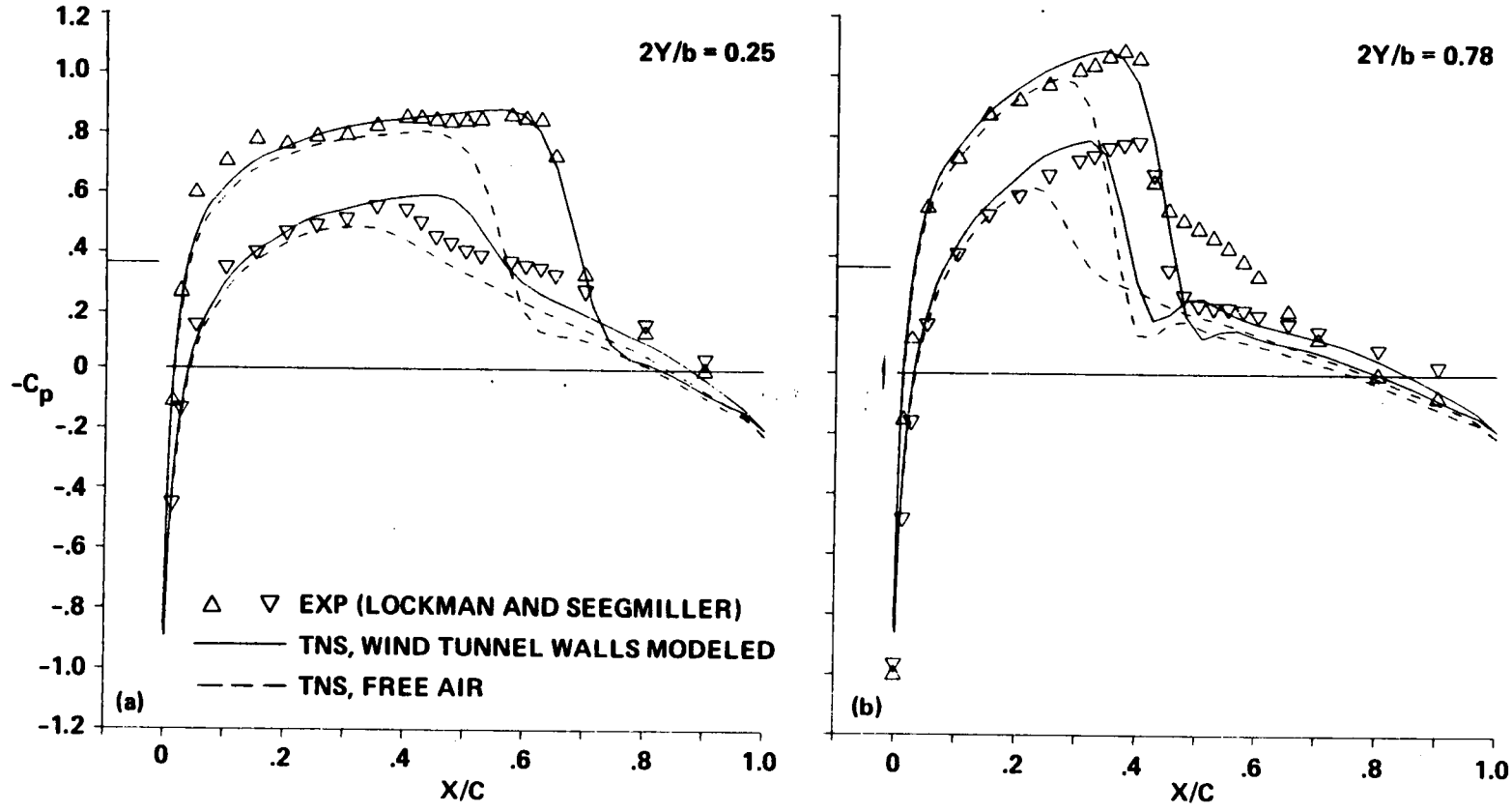
2Y/b = 0.25
2Y/b = 0.78
-Cp
X/C
(a)
(b)
EXP (LOCKMAN AND SEEGMILLER)
TNS, WIND TUNNEL WALLS MODELED
TNS, FREE AIR
1.2
1.0
.8
.6
.4
.2
0
-.2
-.4
-.6
-.8
-1.0
-1.2
.2
.4
.6
1.0

Fig. 7

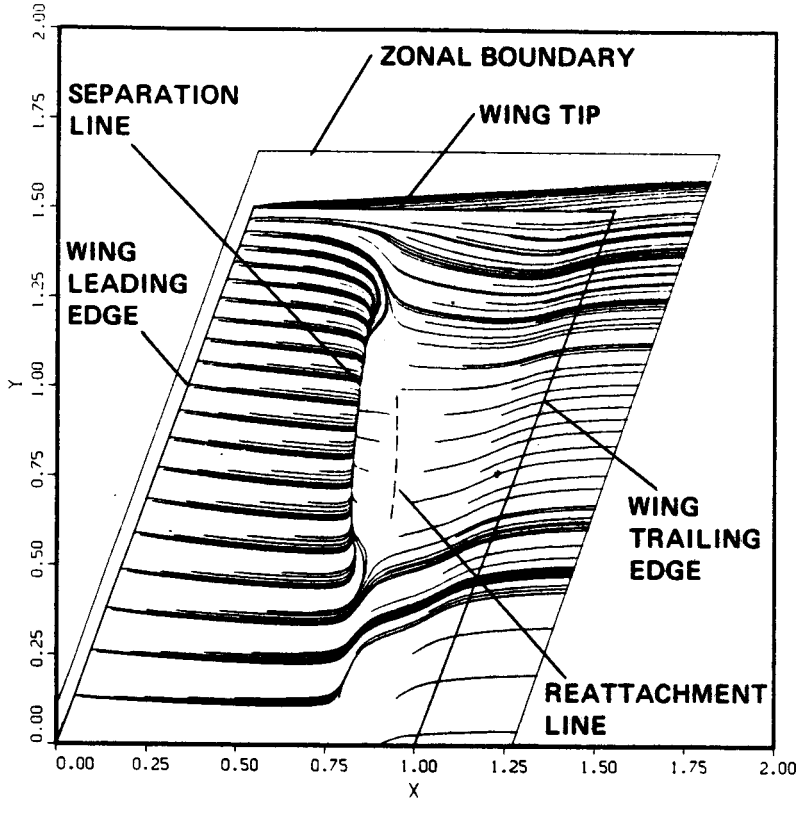
ZONAL BOUNDARY
SEPARATION LINE
WING TIP
WING LEADING EDGE
WING TRAILING EDGE
REATTACHMENT LINE
Y
X
0.00
0.25
0.50
0.75
1.00
1.25
1.50
1.75
2.00

Fig. 8

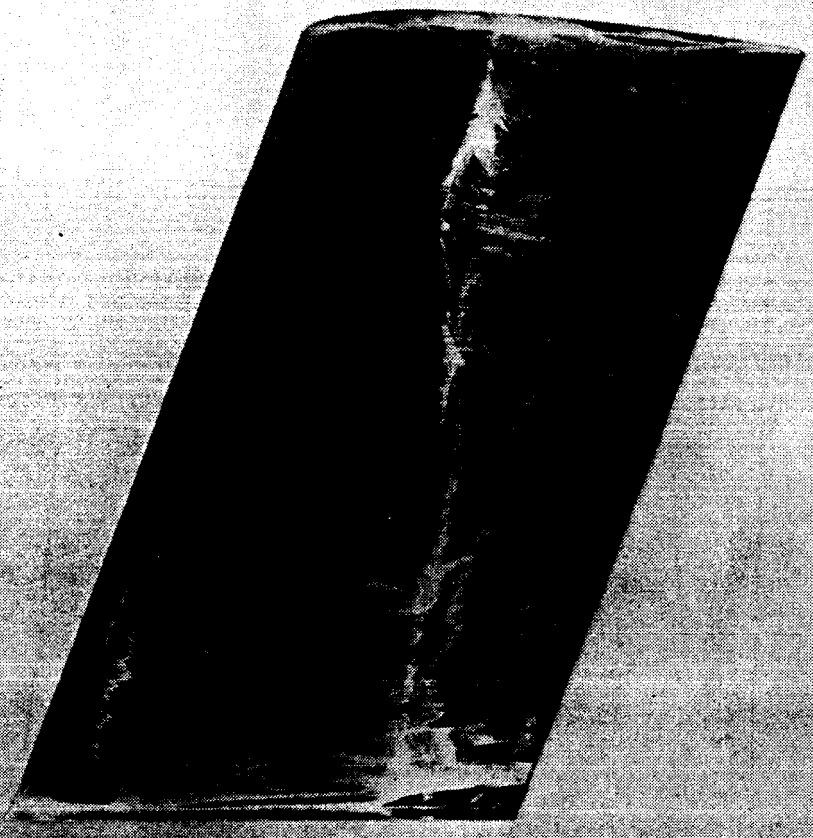

Fig. 9

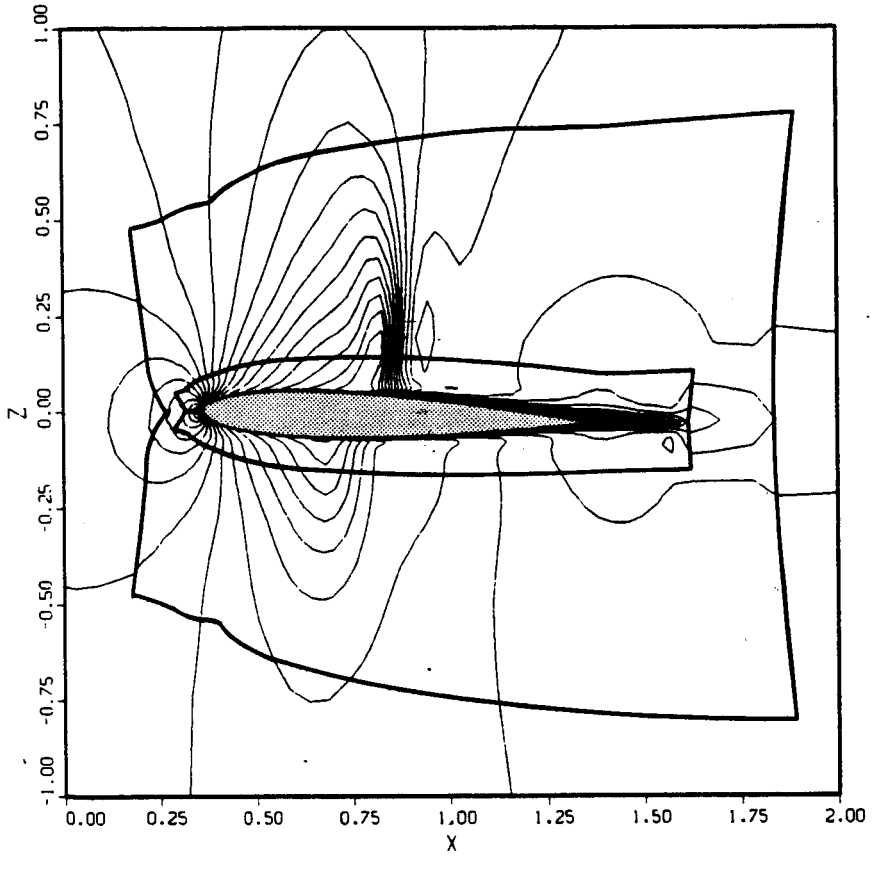

Fig. 10

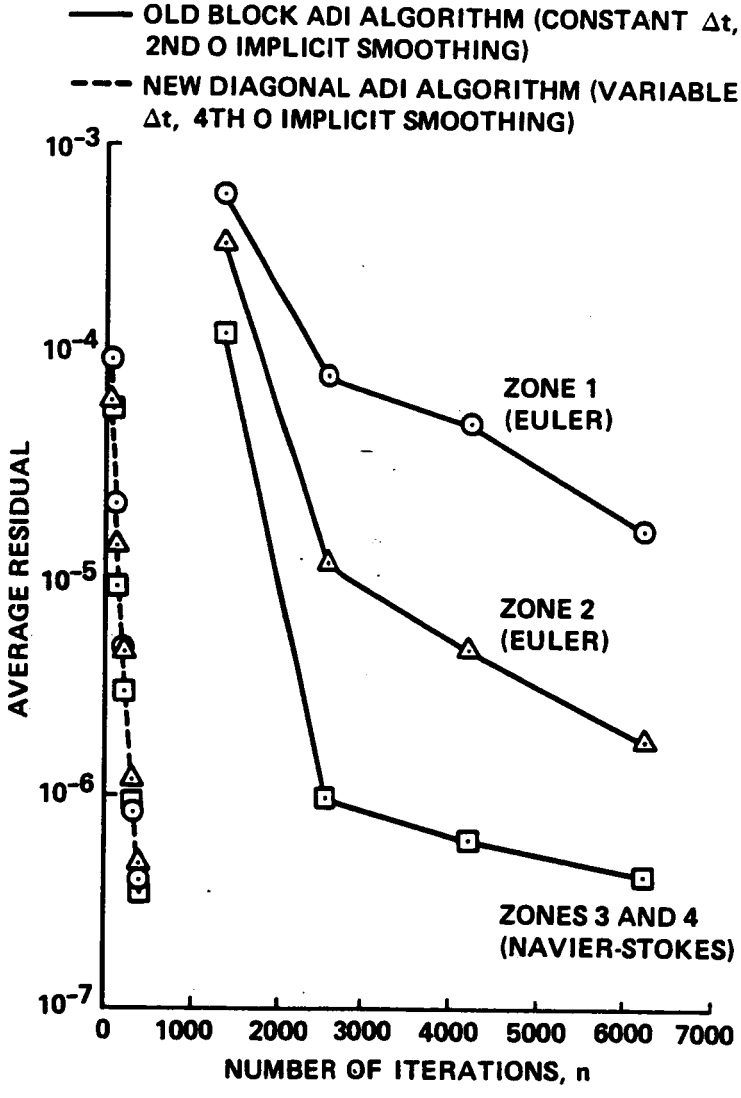
OLD BLOCK ADI ALGORITHM (CONSTANT Δt, 2ND O IMPLICIT SMOOTHING)
NEW DIAGONAL ADI ALGORITHM (VARIABLE Δt, 4TH O IMPLICIT SMOOTHING)
AVERAGE RESIDUAL
10^-3
10^-4
10^-5
10^-6
10^-7
ZONE 1 (EULER)
ZONE 2 (EULER)
ZONES 3 AND 4 (NAVIER-STOKES)
0
1000
2000
3000
4000
5000
6000
7000
NUMBER OF ITERATIONS, n

Fig. 11

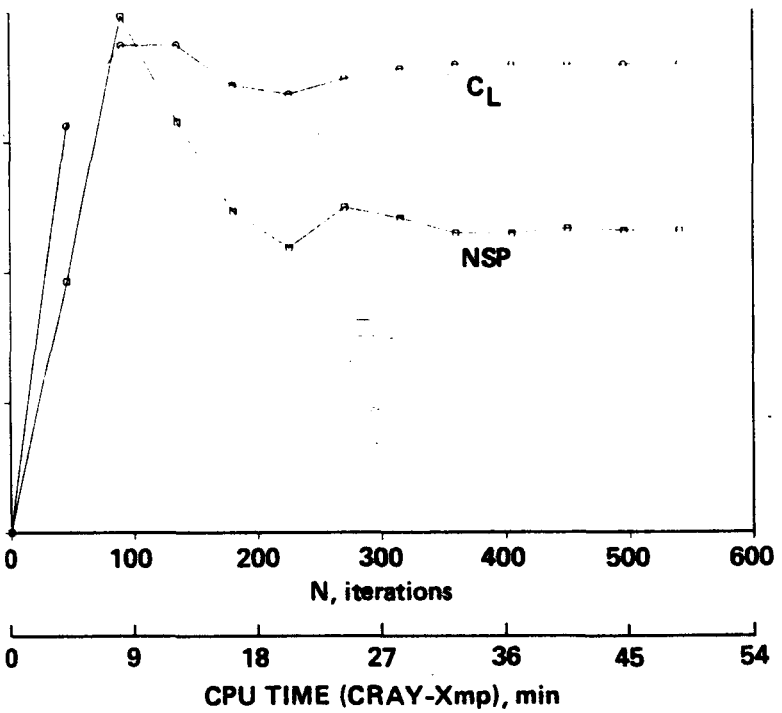
C_L
NSP
0
100
200
300
400
500
600
N, iterations
0
9
18
27
36
45
54
CPU TIME (CRAY-Xmp), min

Fig. 12

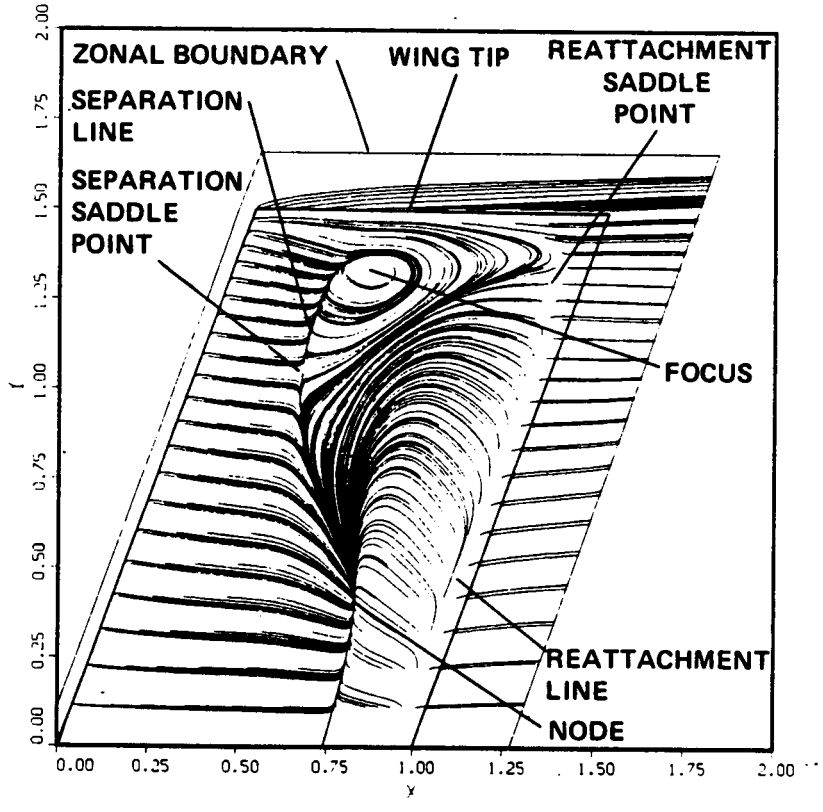

Fig. 13

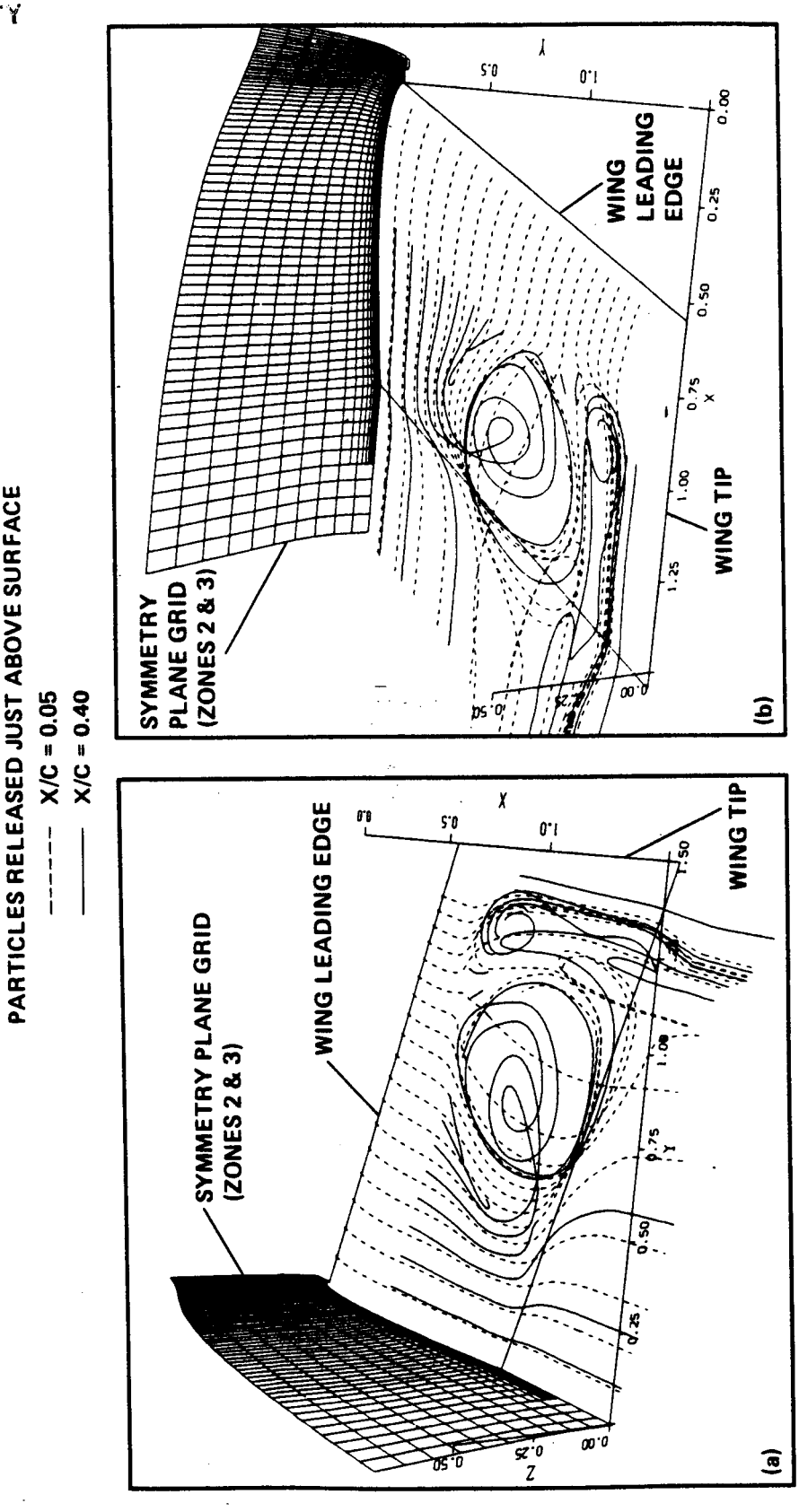

Fig. 14

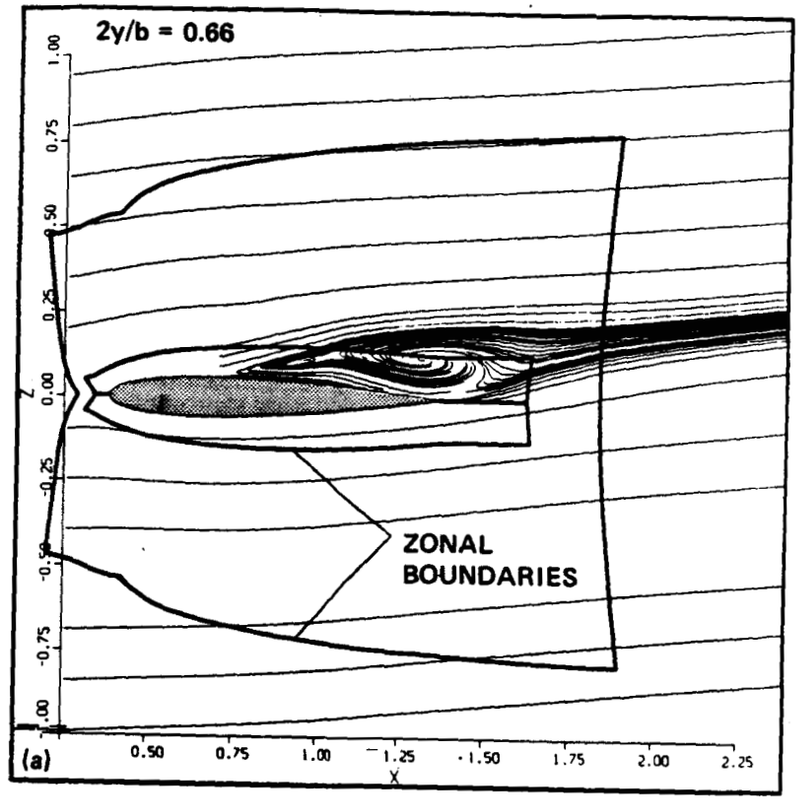

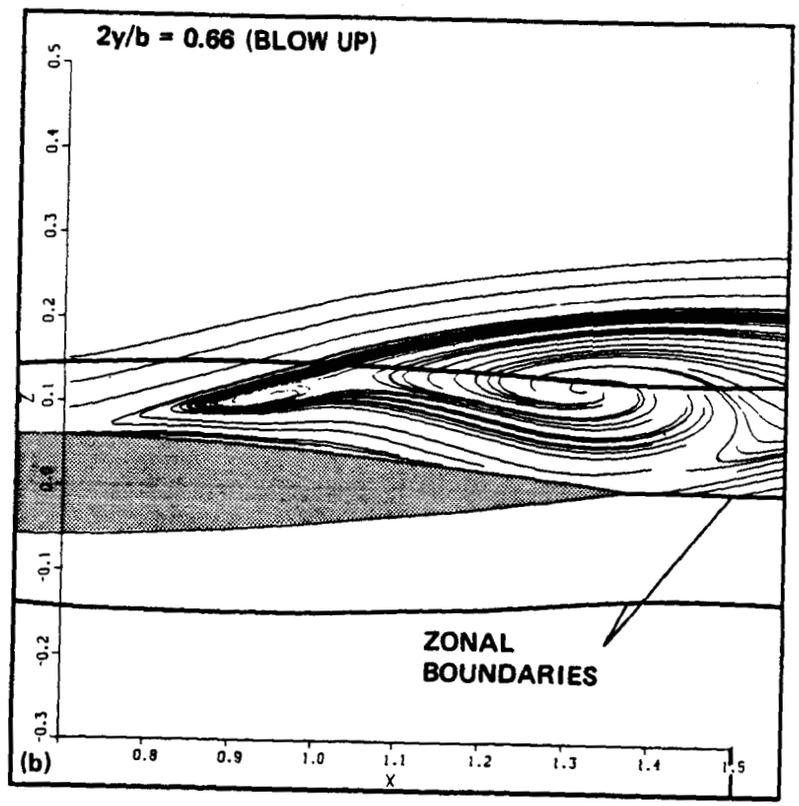

Fig. 15

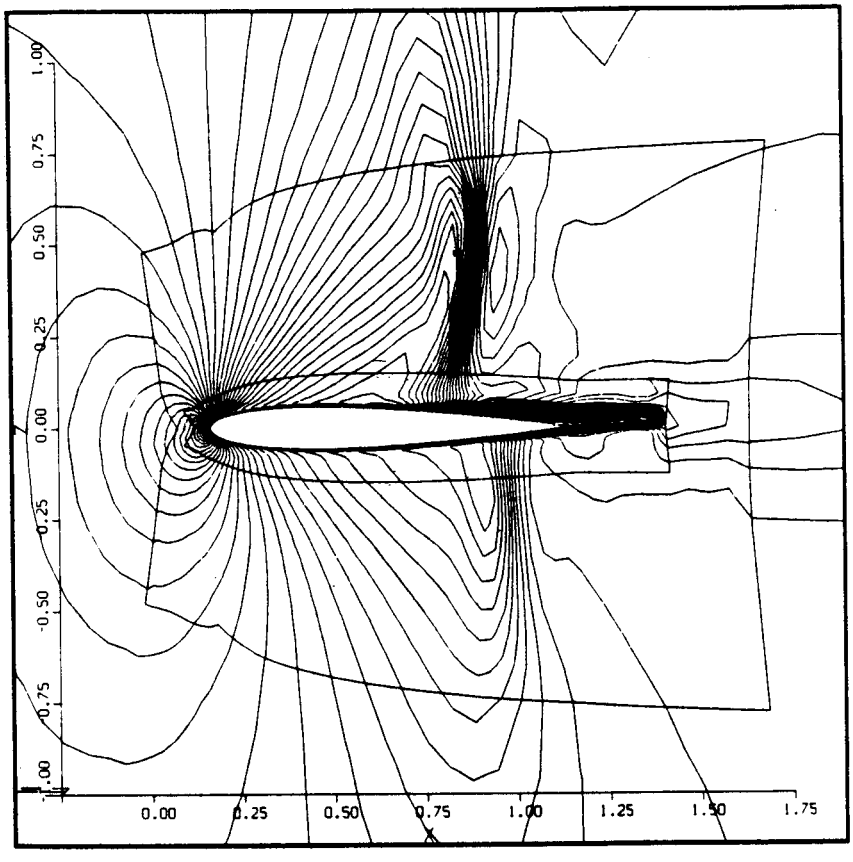
1.00
0.75
0.50
0.25
0.00
-0.25
-0.50
-0.75
-1.00
0.00
0.25
0.50
0.75
1.00
1.25
1.50
1.75

Fig. 16

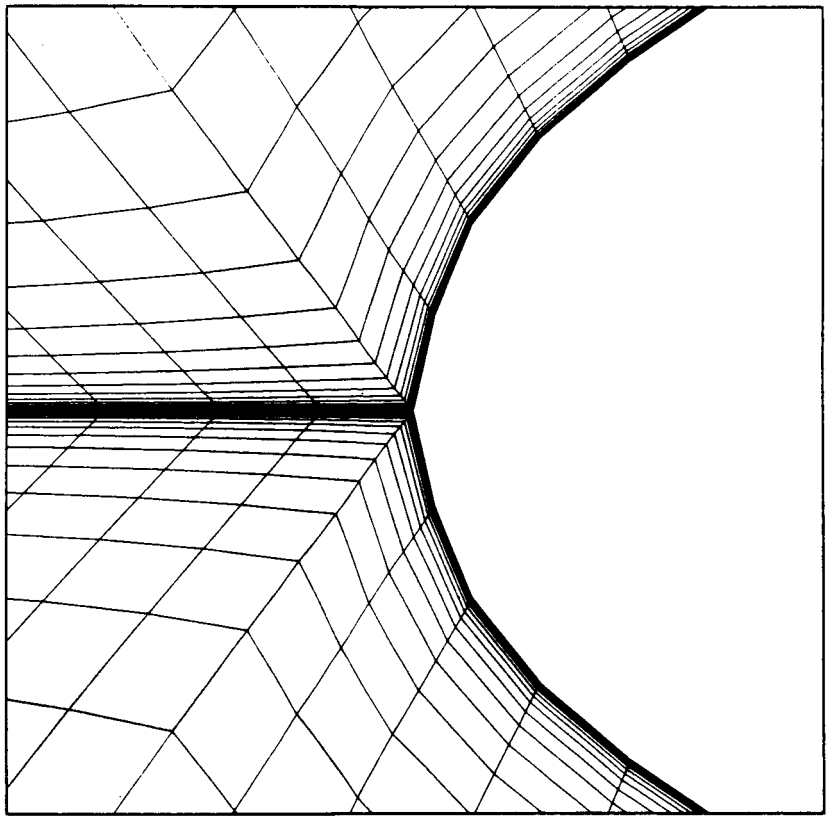

Fig. 17

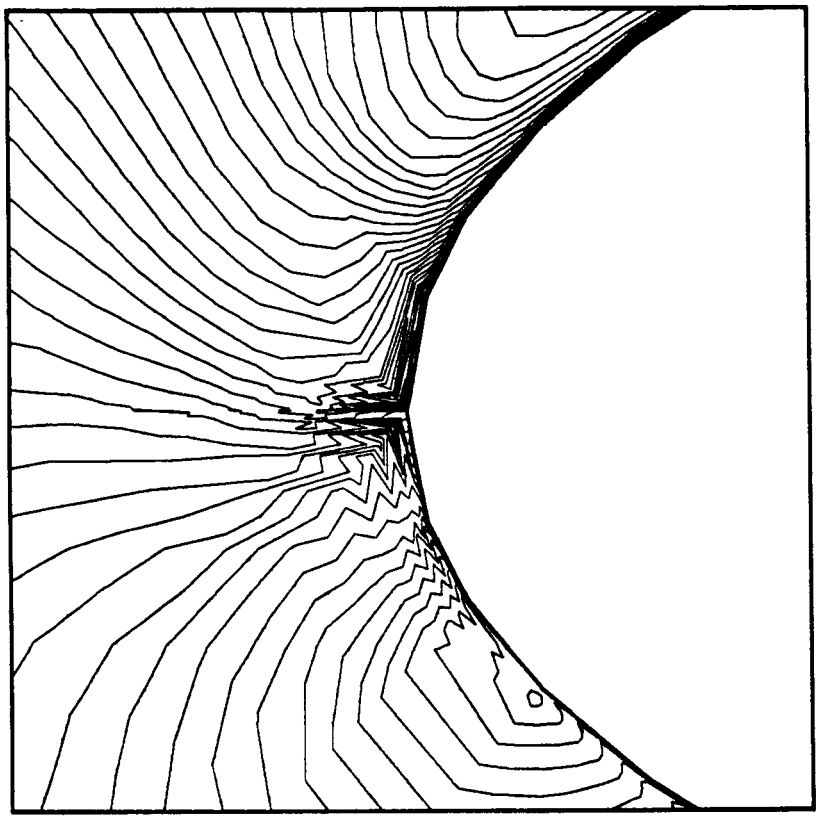

Fig. 18

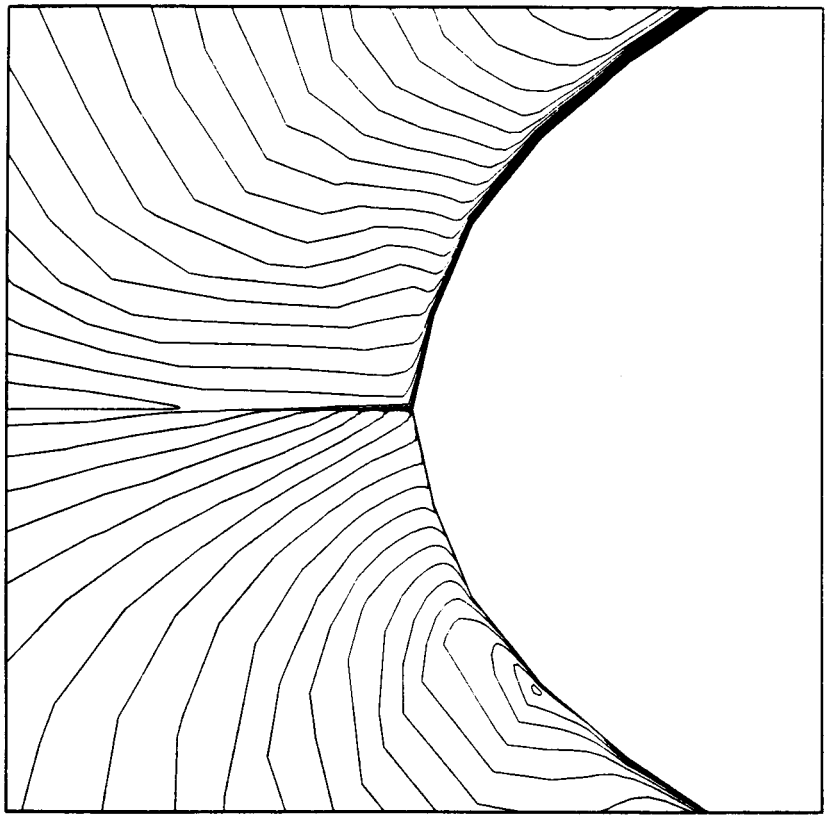

Fig. 19

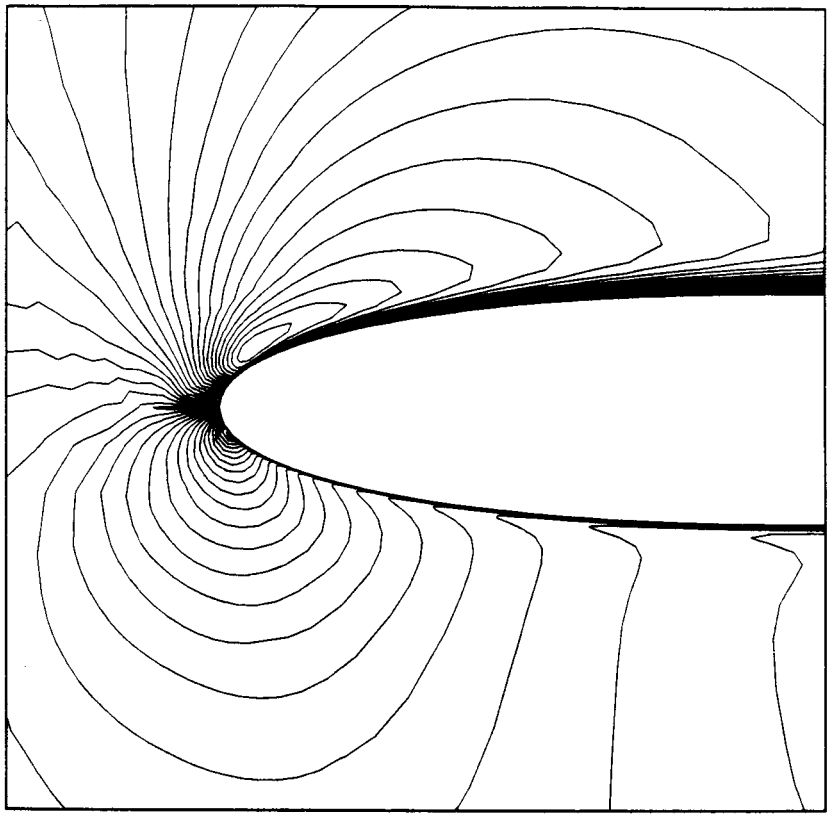

Fig. 20

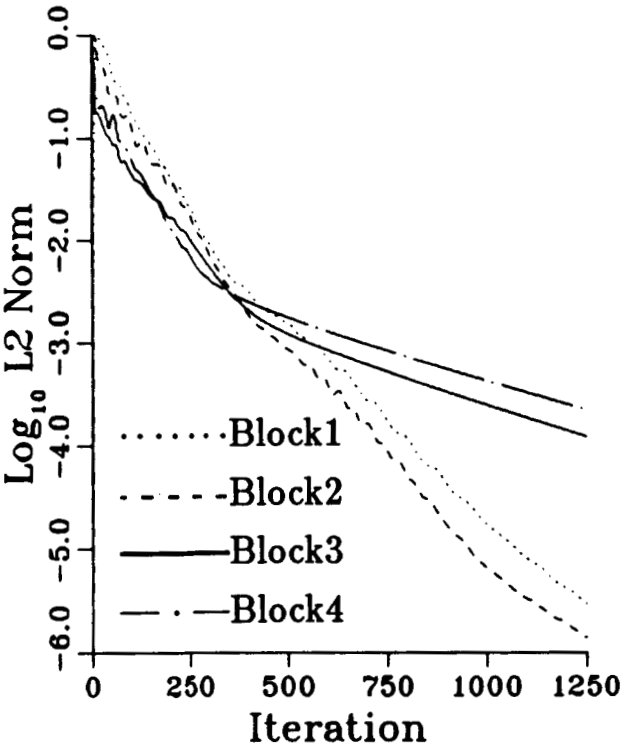
Log10 L2 Norm
0.0
-1.0
-2.0
-3.0
-4.0
-5.0
-6.0
Block1
Block2
Block3
Block4
0
250
500
750
1000
1250
Iteration

Fig. 21

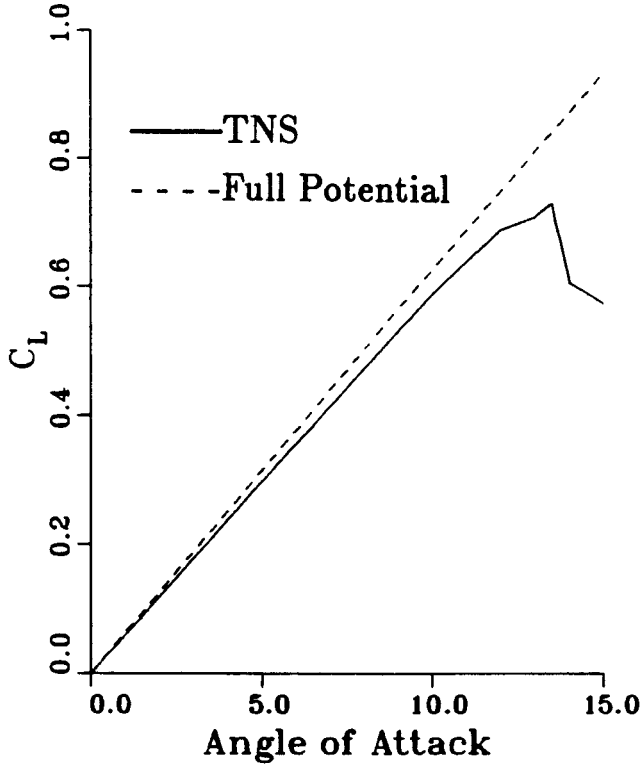
TNS
Full Potential
C_L
0.0
0.2
0.4
0.6
0.8
1.0
0.0
5.0
10.0
15.0
Angle of Attack

Fig. 22

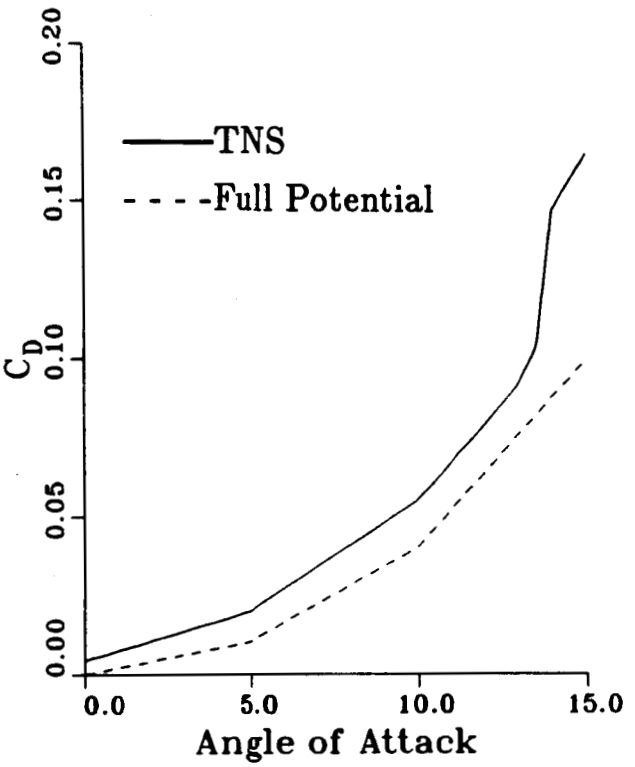
TNS
Full Potential
C_D
0.00
0.05
0.10
0.15
0.20
0.0
5.0
10.0
15.0
Angle of Attack

Fig. 23

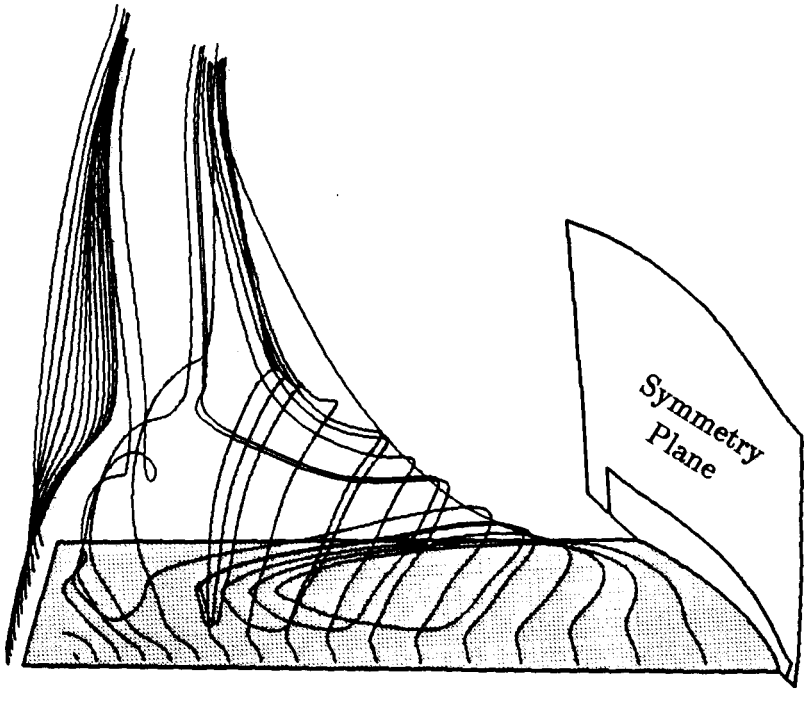

Fig. 24

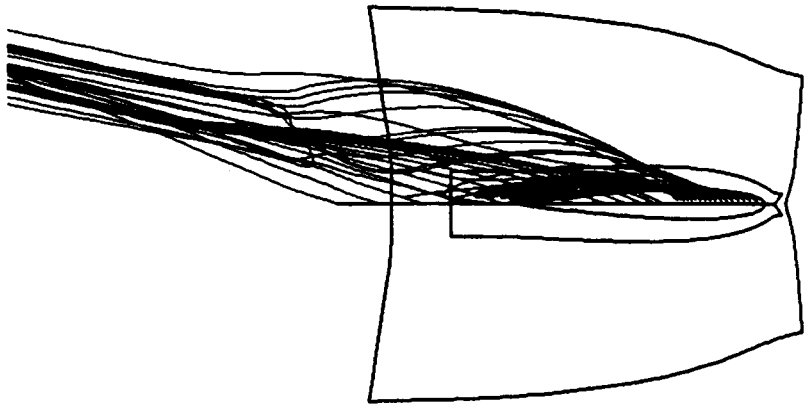

Fig. 25

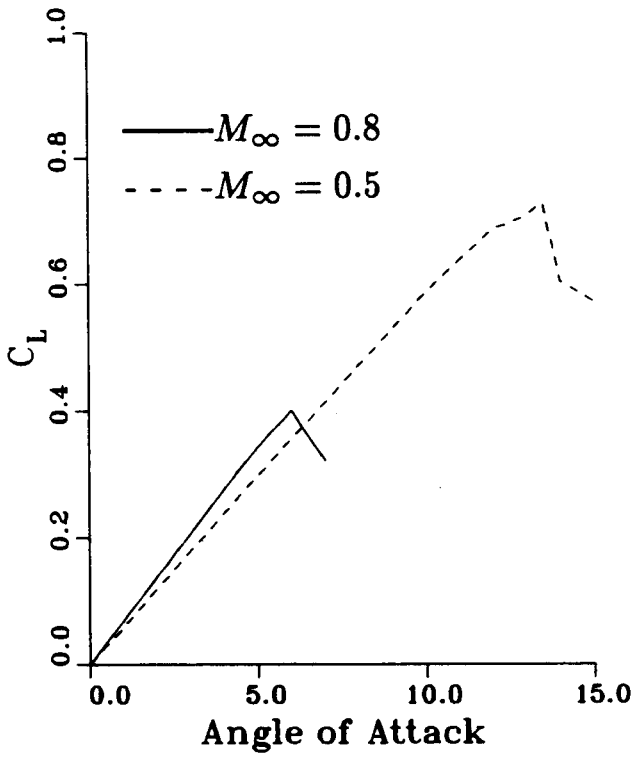
$M_\infty = 0.8$
$M_\infty = 0.5$
C_L
0.0
0.2
0.4
0.6
0.8
1.0
0.0
5.0
10.0
15.0
Angle of Attack

Fig. 26

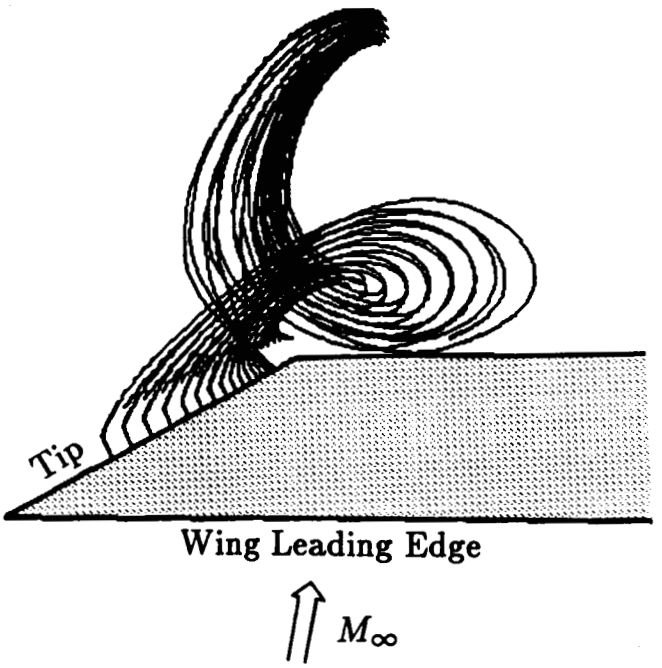

Fig. 27

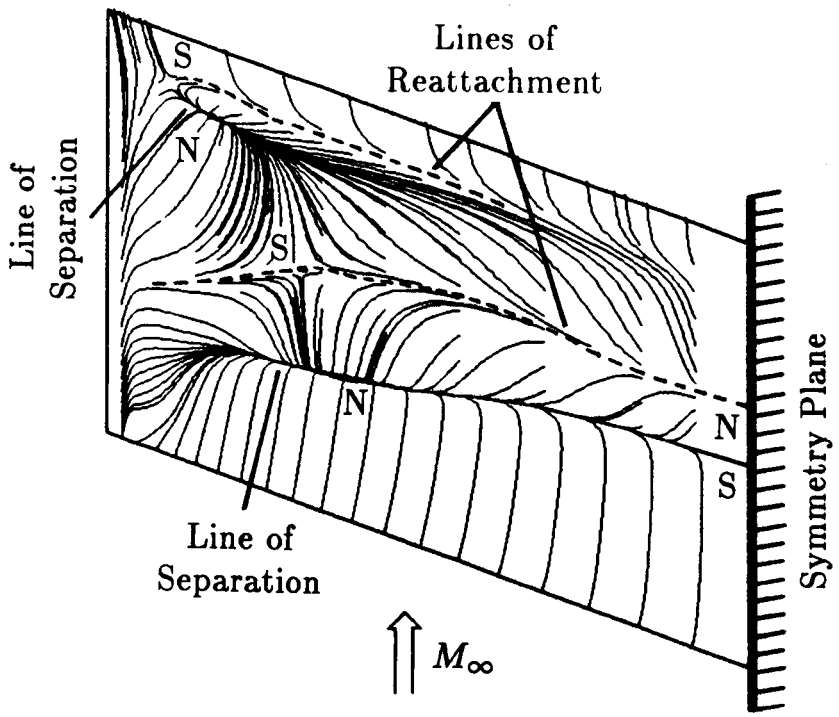
Lines of
Reattachment
S
N
Line of
Separation
S
N
N
S
Symmetry Plane
Line of
Separation
M_∞

Fig. 28

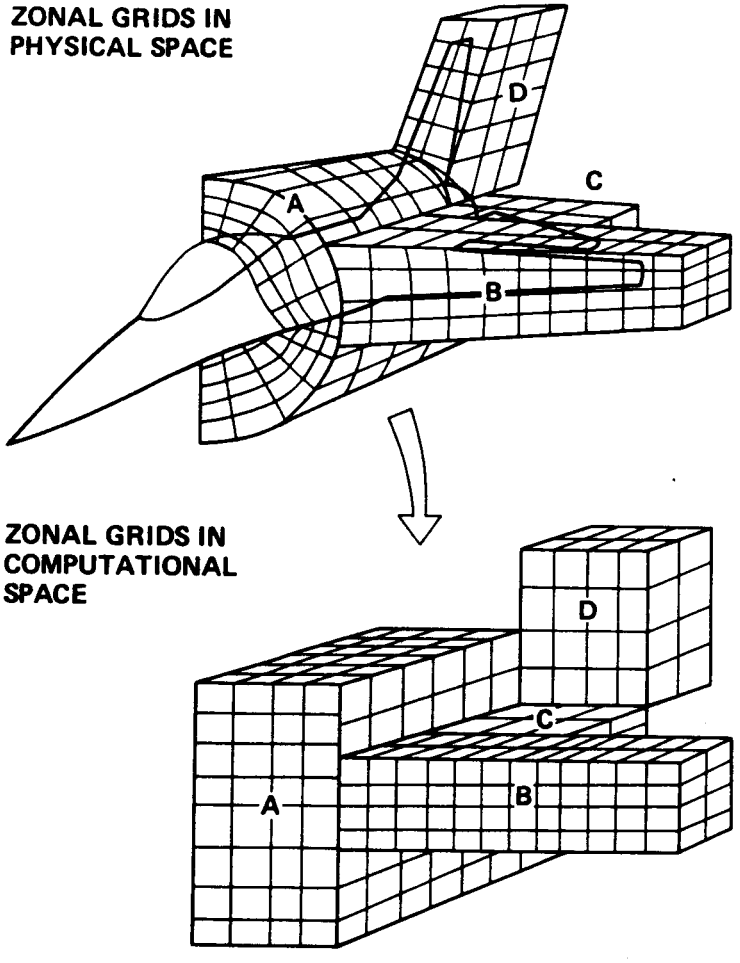

Fig. 29

ELLIPTIC BASE GRID

- O-H TOPOLOGY
- 60 × 20 × 24

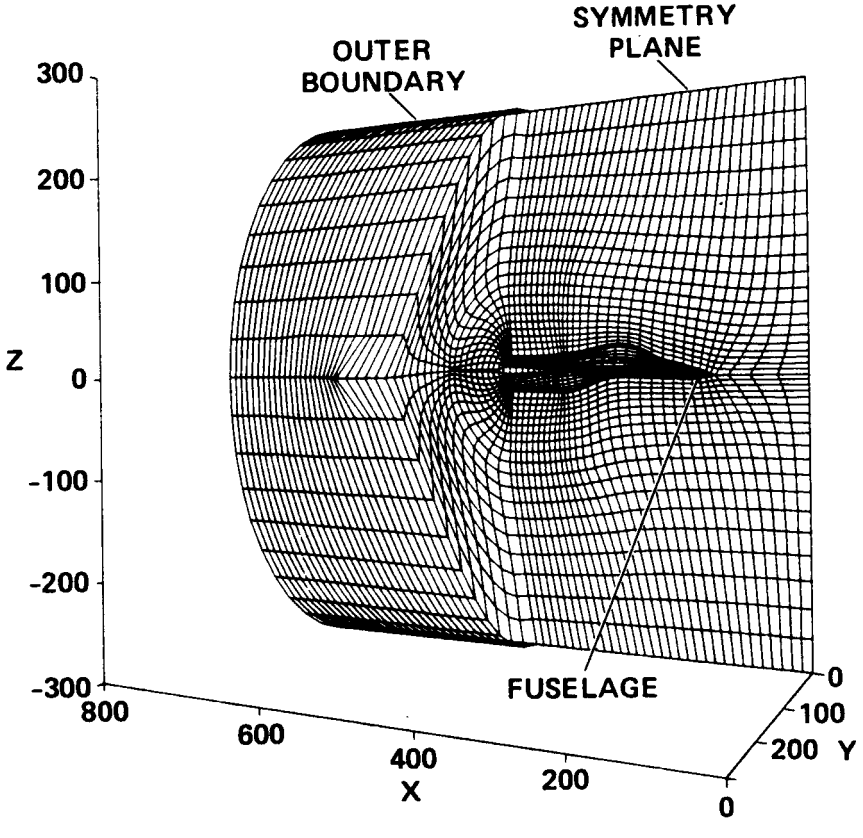

Fig. 30

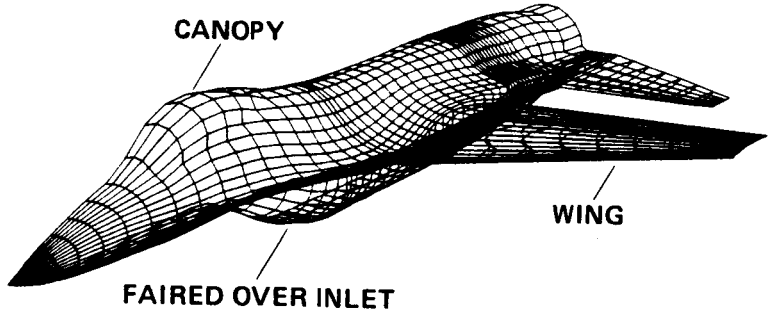

(a)

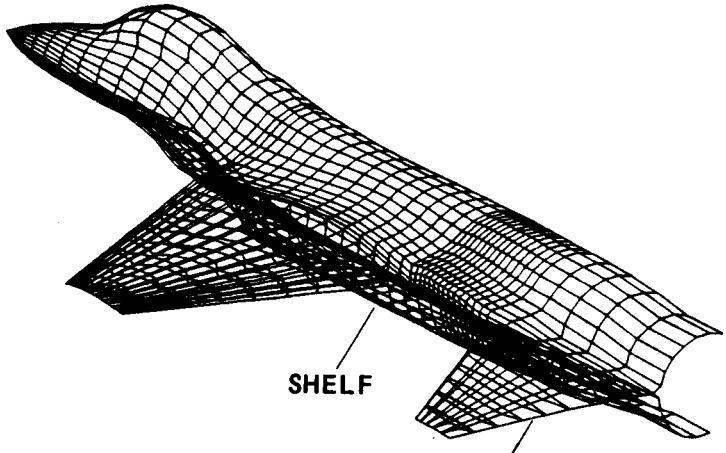

(b)

Fig. 31

BASE GRID PLANFORM

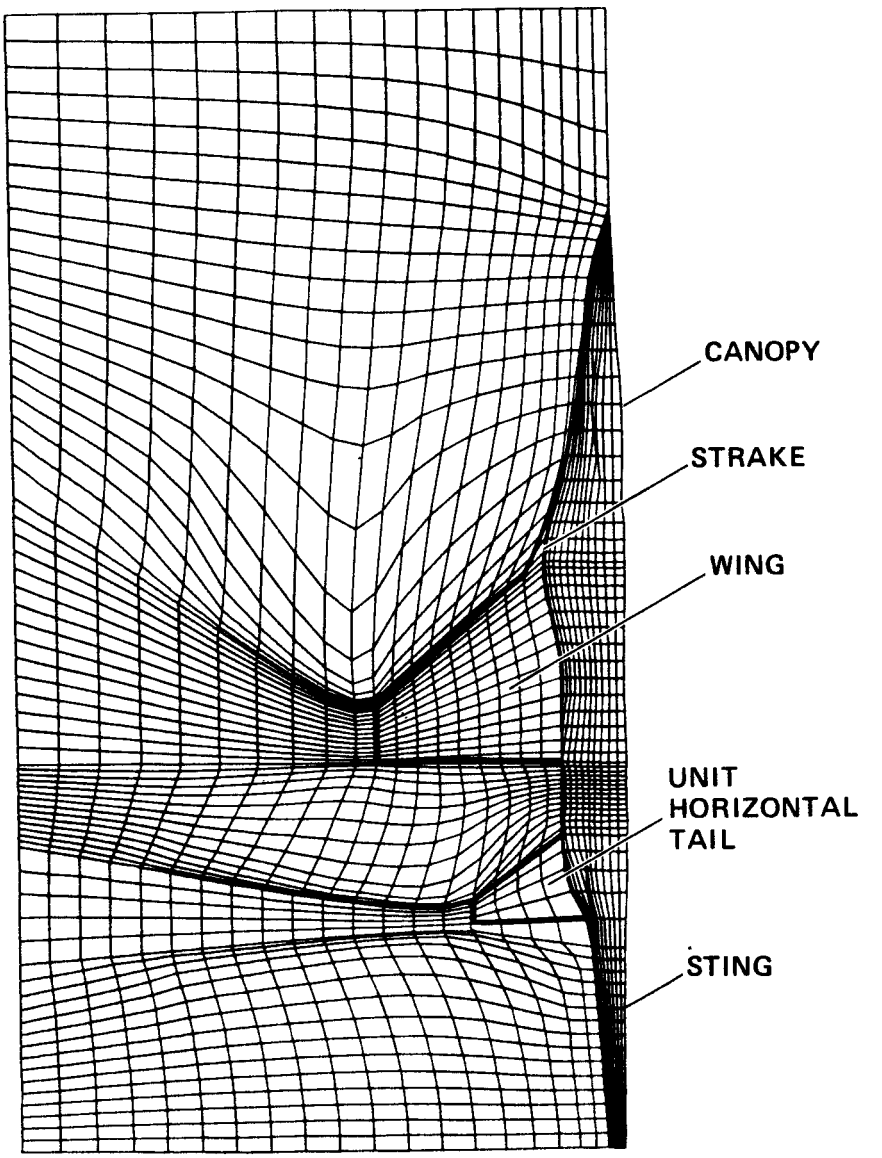

Fig. 32

F-16A ZONAL SCHEMATIC

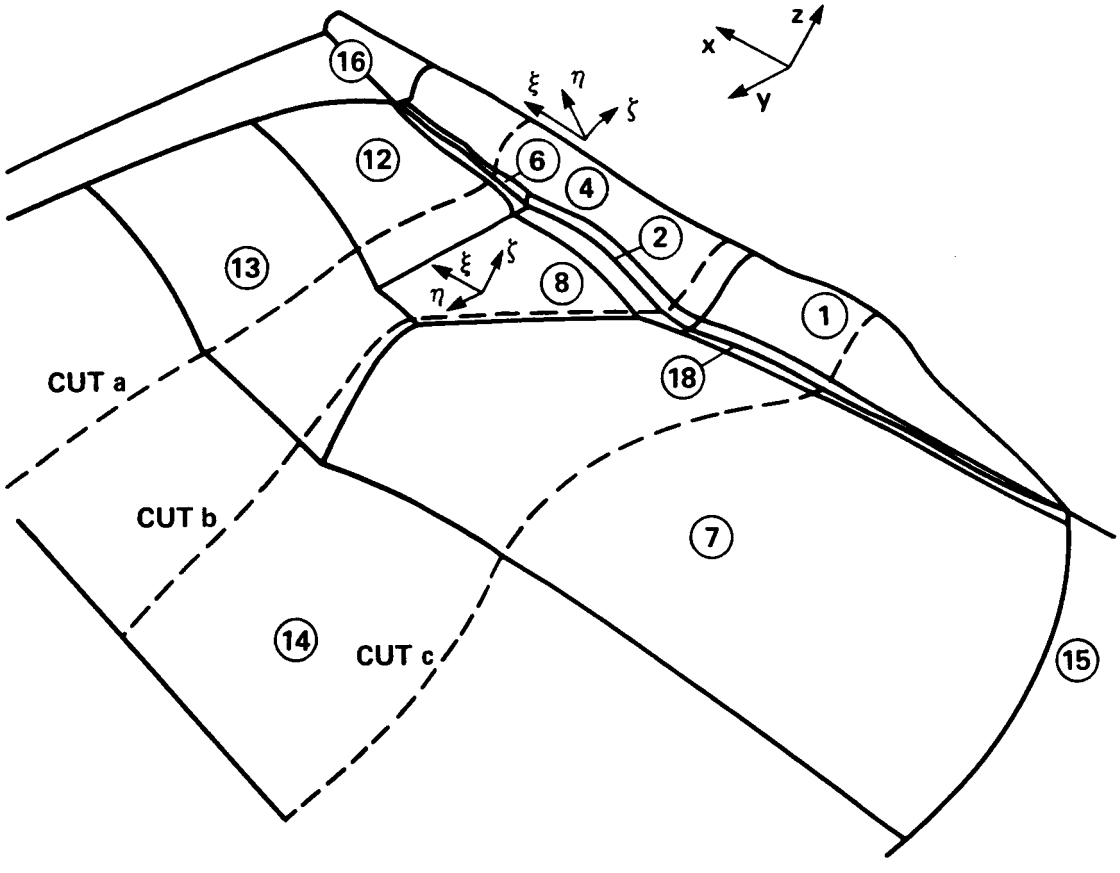

Fig. 33

WING FUSELAGE MESH TOPOLOGIES

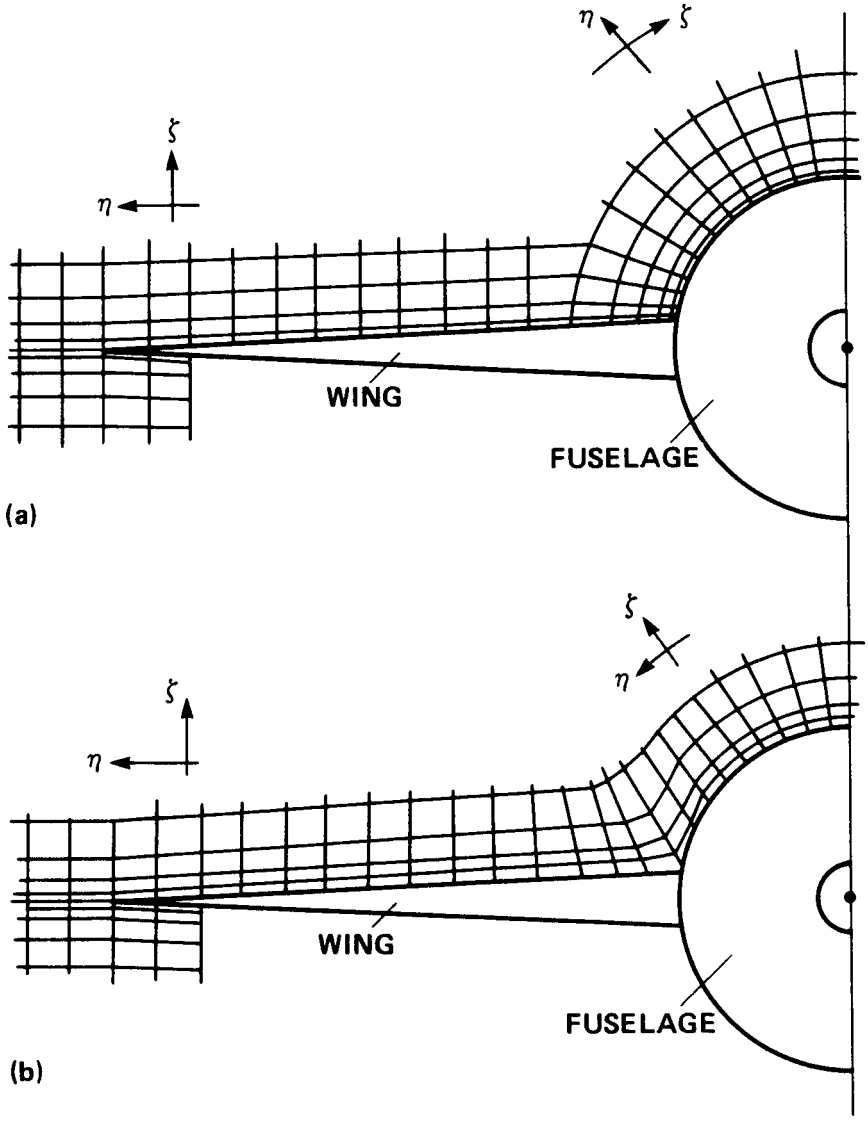

Fig. 34

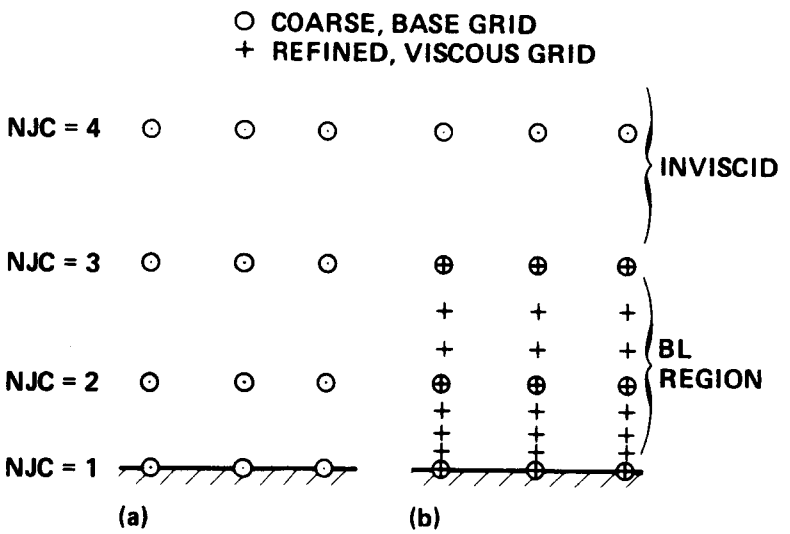
O COARSE, BASE GRID
+ REFINED, VISCOUS GRID
NJC = 4
NJC = 3
NJC = 2
NJC = 1
INVISCID
BL
REGION
(a)
(b)

Fig. 35

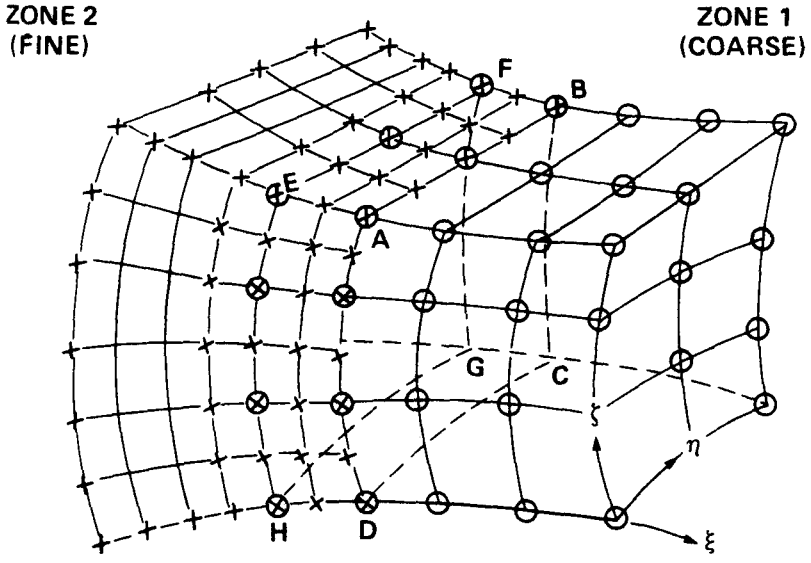

(a) TWO-ZONE GRID SHOWING OVERLAP AT ABCD AND EFGH PLANES IN PHYSICAL SPACE

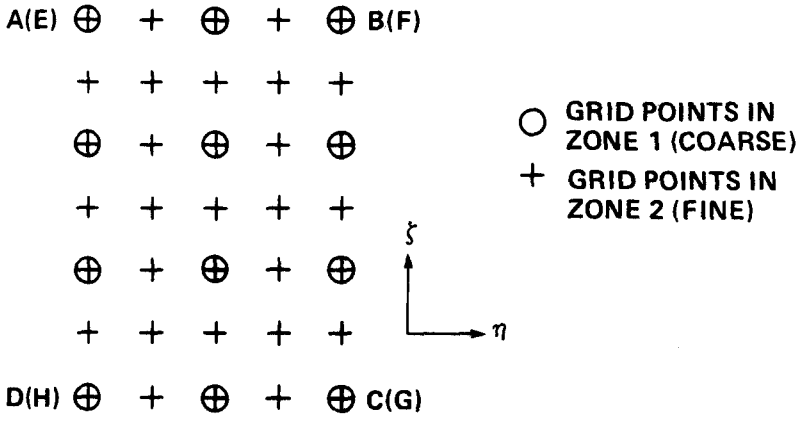

(b) GRID POINT DETAIL IN THE OVERLAP REGION IN TRANSFORMED SPACE

Fig. 36

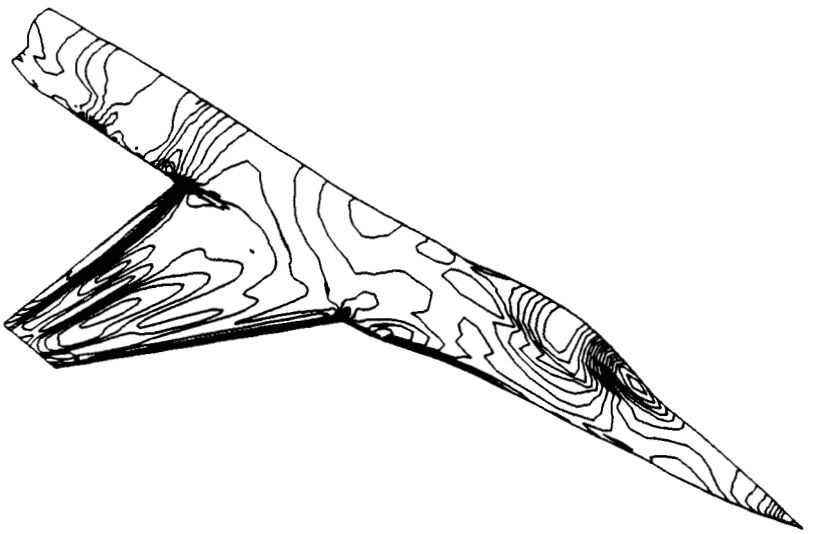

Fig. 37

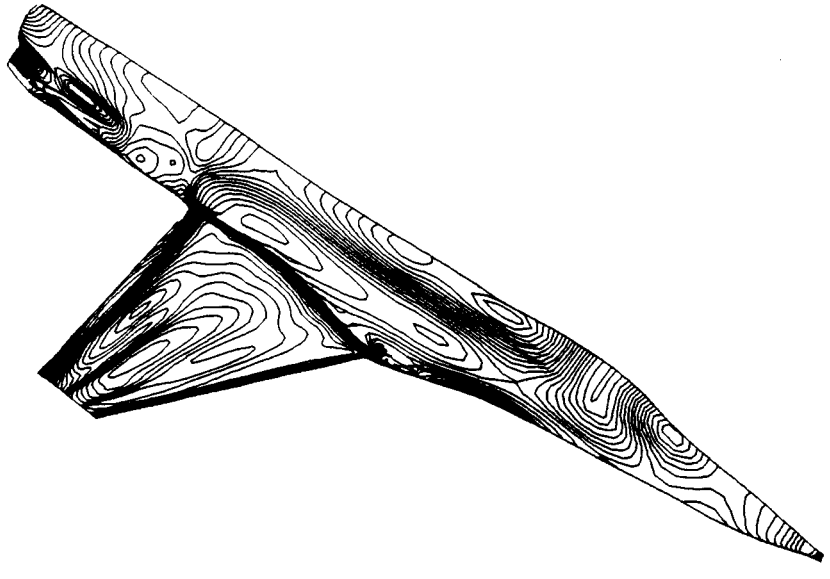

Fig. 38

NASA
National Aeronautics and Space Administration

Report Documentation Page

1. Report No.	2. Government Accession No.	3. Recipient's Catalog No.
NASA TM 89421		

4. Title and Subtitle	5. Report Date
Simulation of Transonic Viscous Wing and Wing-Fuselage Flows Using Zonal Methods	March 1987
	6. Performing Organization Code

7. Author(s)	8. Performing Organization Report No.
Jolen Flores	A87066
	10. Work Unit No. 505-60-01

9. Performing Organization Name and Address	11. Contract or Grant No.
Ames Research Center Moffett Field, CA, 94035	
	13. Type of Report and Period Covered
12. Sponsoring Agency Name and Address	Technical Memorandum
National Aeronautics and Space Administration Washington, DC 20546	14. Sponsoring Agency Code

15. Supplementary Notes

Point of contact: Jolen Flores, Ames Research Center, MS 202A-14, Moffett Field, California 94035 (415) 694-5369 or FTS 464-5369

16. Abstract

The thin-layer Navier-Stokes equations are coupled with a zonal scheme (or domain-decomposition method) to develop the Transonic Navier-Stokes (TNS) wing-alone code. TNS has a total of 4 zones and is extended to a total of 16 zones for the wing-fuselage version of the code. Results are computed on the Cray X-MP-48 and compared with experimental data.

17. Key Words (Suggested by Author(s))	18. Distribution Statement
Zonal Wing/fuselage Transonic	Unclassified - Unlimited

19. Security Classif. (of this report)	20. Security Classif. (of this page)	21. No. of pages	22. Price
Unclassified	Unclassified	68	A04

For sale by the National Technical Information Service, Springfield, Virginia 22161